Chapter 6

The rapid scintillator, PKS 1257−326

> "...the data presented in Figures 1–3 are of such extraordinary quality that they look like outputs of a simulation. Together with similar recent reports for other quasars by many of the same authors, this work may herald a new era in studies of the local ionized interstellar medium, and perhaps of also of the small-scale structure in compact extragalactic radio sources."
>
> **Anonymous referee**

A large part of the work presented in this chapter has been accepted for publication in *The Astrophysical Journal* (to appear on March 10, 2003):
Rapid Variability and Annual Cycles in the Characteristic Time-scale of the Scintillating Source PKS 1257−326, H. E. Bignall, D. L. Jauncey, J. E. J. Lovell, A. K. Tzioumis, L. Kedziora-Chudczer, J.-P. Macquart, S. J. Tingay, D. P. Rayner, and R. W. Clay.

6.1 Abstract

This chapter presents results of the ATCA observations described in Chapter 5 for the quasar PKS 1257−326. The very rapid variability of PKS 1257−326 makes it an ideal target for "Earth Orbit Synthesis" (Macquart & Jauncey, 2002), because it is possible to characterise the variability accurately in a typical 12-hour observing session. A clear *annual cycle* has been observed in the characteristic time-scale for this source. Furthermore, a time delay of several minutes was observed between the variability pattern arrival times at two widely separated telescopes, the NRAO's Very Large Array (VLA) in New Mexico, and the ATCA. Both the annual cycle and the time delay provide unequivocal evidence that the very rapid variability observed in the radio emission from PKS 1257−326 is due primarily to interstellar scintillation (ISS). From both of these sets of observations, it is possible to derive the scale of the scintillation pattern and the velocity of the scattering material, and hence to constrain the source angular size and the distance to the scattering plasma. Most scintillating

sources have longer characteristic time-scales and therefore data over several days are required to accurately estimate the time-scale and amplitude of the variability. Likely reasons for the rapid variability observed in PKS 1257−326 are discussed in Section 6.7. The scintillation of this source has been used as a unique probe of microarcsecond-scale source structure.

6.2 The PKS 1257−326 story

PKS 1257−326 was first catalogued in the Sixth Part of the Parkes 2700 MHz Survey (Shimmins & Bolton, 1974), with a measured flux density of 0.23 Jy at 2.7 GHz. It was also found in the PMN Survey (Wright et al., 1996) with a 5 GHz flux density of 0.24 Jy. Rapid variability was discovered in PKS 1257−326 in 2000. In early 2000, a multi-source dataset from ATCA observations in October 1995 was re-analysed as part of a separate project, the Deep X-ray Radio Blazar Survey (DXRBS; Perlman et al. 1998; Landt et al. 2001). PKS 1257−326 was identified in the DXRBS as a flat-spectrum radio and X-ray emitting quasar at $z = 1.256$. It has optical magnitude $B = 18.7$ and has been detected at X-ray energies with the ROSAT PSPC (Position-Sensitive Proportional Counter) detector, emitting 2×10^{-13} erg cm^{-2} s^{-1} between 0.1 and 2.0 keV (Perlman et al., 1998). Unlike the more "famous", brighter blazars, very few observations of PKS 1257−326 are previously recorded in the literature.

Two brief, 1-minute cuts on PKS 1257−326 on October 12, 1995, separated by ~ 6 hours, showed the flux density to be substantially different in each cut. Visibilities for all sources observed with the ATCA as part of the DXRBS ($\sim$ 300 sources in total) were examined, but no such change was observed for any of the other sources. Plotted in Figure 6.1 is the amplitude of the PKS 1257−326 visibilities versus (u, v) distance at 4.8 GHz, which clearly shows the ~ 40 mJy separation of the two cuts. The slight increase in flux density towards shorter (u, v) spacings indicates weak extended emission, contributing $\sim$ 20 mJy to the total flux density, in addition to a much stronger, unresolved component. This is consistent with what is found from a later VLA image of the source (see Section 6.3.3). However, structure is evidently not the cause of the difference in average flux density between the two cuts. The observations were at 4.8 and 8.6 GHz, and a similar change in flux density of ~ 25 mJy was evident at 8.6 GHz.

In June 2000, 6 cuts on PKS 1257−326 were obtained during the final epoch of the ATCA blazar monitoring observations (project C639) described in Chapter 3. These observations confirmed the presence of IDV in the source. Another observation was obtained in September 2000 as a Target of Opportunity during unallocated time on the ATCA. The significance of the IDV in PKS 1257−326 was now appreciated. An ATCA proposal was submitted in October, and the monitoring program described in Chapter 5 commenced in February 2001. In the first observing session, the rapid variability in PKS 1257−326 was undersampled, indicating that the characteristic time-scale had significantly decreased since the observations in September 2000. A separate, short observing session on PKS 1257−326 alone was obtained on 28 February. Flux density

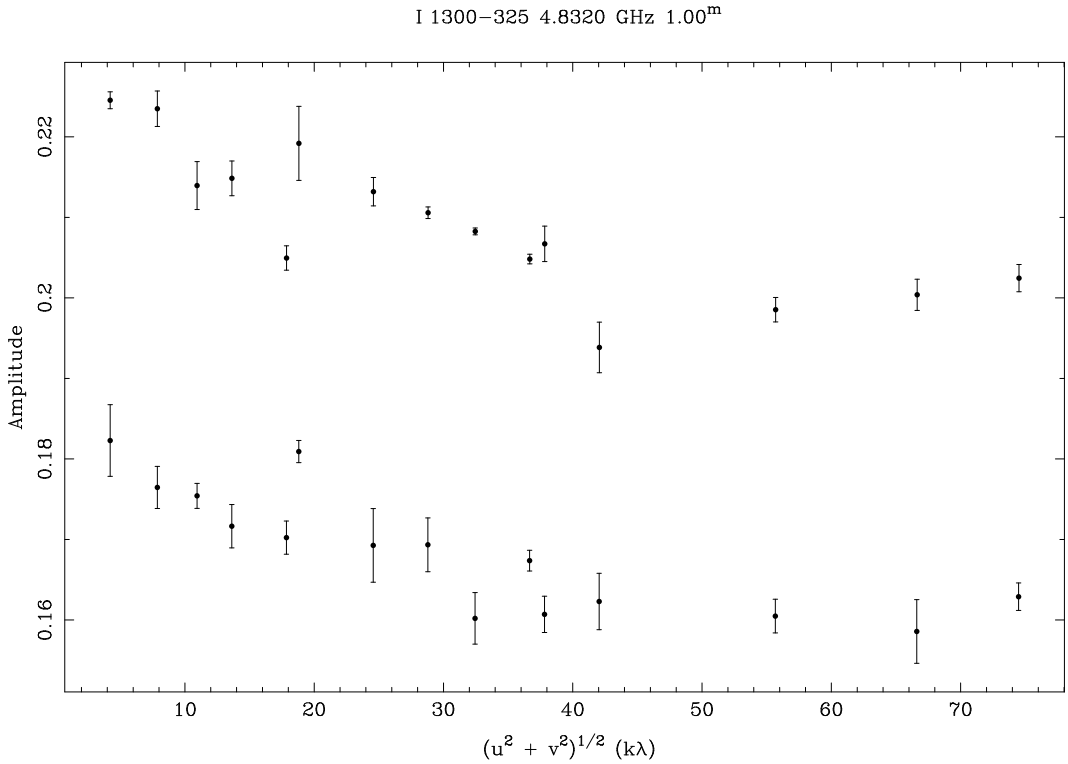

Figure 6.1: Data on PKS 1257−326 from two short cuts, separated by ~ 6 hours, observed on October 12, 1995, which were re-analysed in 2000. Visibility amplitudes at 4.8 GHz, averaged over the scan for each baseline, are plotted as a function of distance in the (u, v) plane.

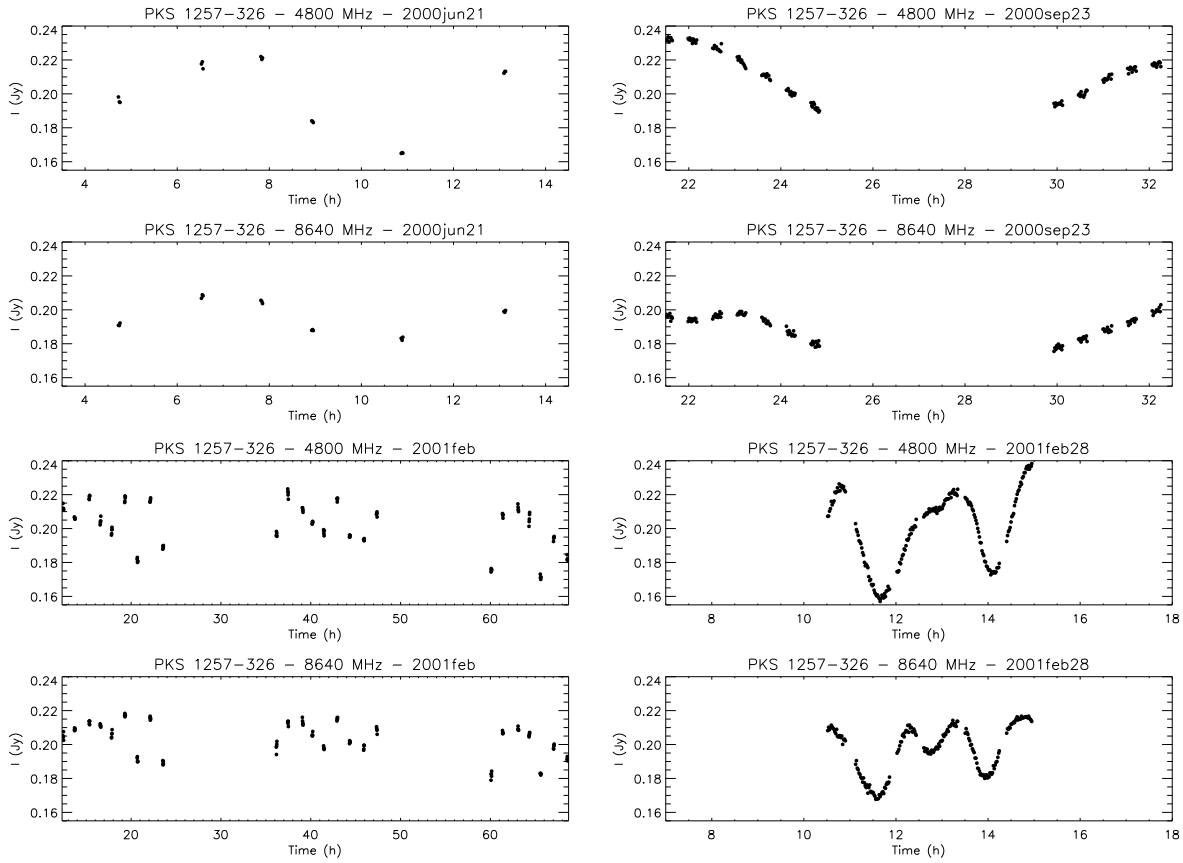

Figure 6.2: ATCA observations of PKS 1257−326 in four early epochs, at 4.8 and 8.6 GHz. There is a clear change in variability time-scale between September 23, 2000, and February 2001, where the rapid variability was undersampled during the 3 day observation in early February. The 4-hour gap in data on September 23, 2000 is due to observations for another project. The vertical scale is the same in all plots; the horizontal scale is the same except for the two lower left windows which cover 3 days, 4–6 February 2001.

measurements from these four early observations are shown in Figure 6.2.

6.2.1 Characteristics of the rapid variability

PKS 1257−326 has shown rapid IDV in every observation between June 2000 and September 2002, and in the earlier data of October 1995. It therefore seems likely that the source has been showing this rapid variability for at least 7 years.

Figure 6.3 shows the remarkably smooth, quasi-periodic nature of the variability at both frequencies, which is described here by a single time-scale parameter, $t_{0.5}$, defined as the half-width at half-maximum of the auto-correlation function (see Section 6.4.1). Also noticeable is the strong similarity between the variations at 4.8 and 8.6 GHz that is a characteristic of many IDV sources, in particular, the other extreme variables, PKS 0405−385 (Kedziora-Chudczer et al., 1997) and J1819+3845 (Dennett-Thorpe &

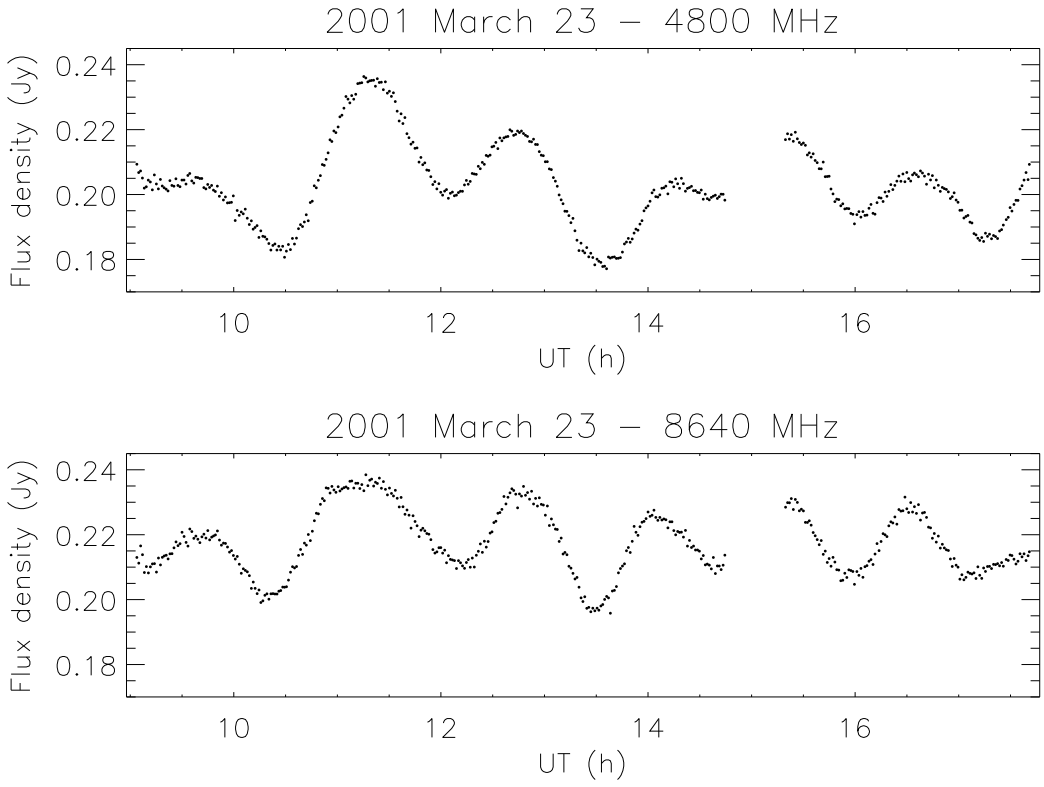

Figure 6.3: ATCA data showing the flux density variations in PKS 1257−326 at 4.8 and 8.6 GHz on 2001 March 23

de Bruyn, 2000).

6.3 Measurement of the pattern time delay between the VLA and ATCA

6.3.1 Background

In late 1998, simultaneous observations of PKS 0405−385 at the ATCA and the VLA showed a convincing time delay of around 2 minutes, between the IDV pattern arrival times at each telescope (Jauncey et al., 2000b), which showed without doubt that ISS was the principal cause of the rapid variability osberved in this source. Observations of J1819+3845 between the WSRT and the VLA also showed a clear time delay in the IDV pattern arrival times at each telescope, which changed over the course of the observation due to the rotation of the projected baseline vector, and enabled the scattering screen velocity to be constrained (Dennett-Thorpe & de Bruyn, 2002). This technique gives direct constraints on the scintillation geometry and velocity, and is of particular value in understanding scattering and structure in the ISM. Similar techniques have been used

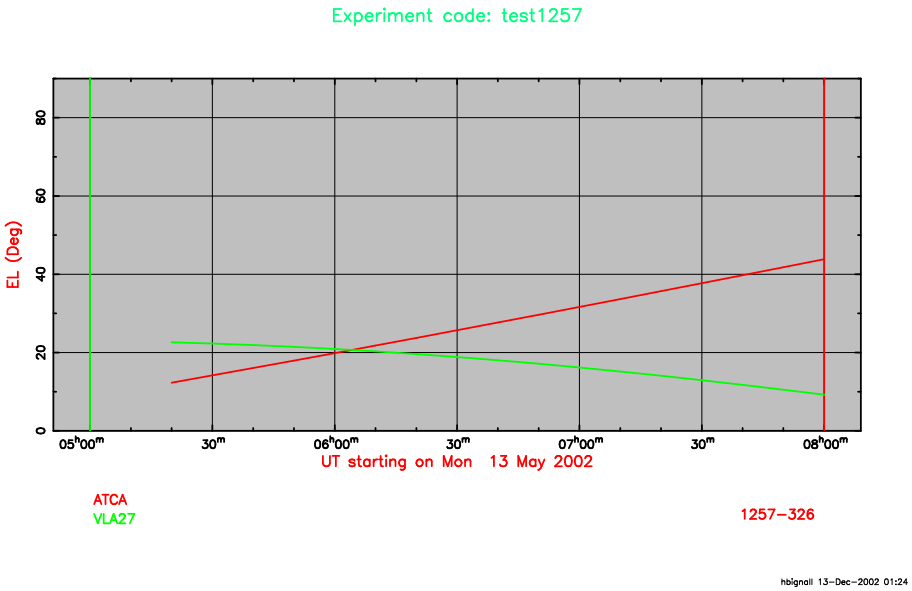

Figure 6.4: Elevation as a function of time for the VLA and ATCA, over the PKS 1257−326 common visibility. The VLA is observing the source at an elevation of $\sim 22°$ when it rises to the elevation limit of the ATCA, and is at an elevation of $\sim 45°$ at the ATCA when the VLA sees it set.

to study interplanetary scintillations (IPS) in weak scattering (e.g. Coles & Kaufman, 1978), and interstellar scintillation of pulsars (e.g. Rickett & Lang, 1973).

In order to properly constrain the delay it is necessary to sample maxima and minima in the light curve, implying that time-scale of the variations must be short. For most scintillating quasars which vary on time-scales of the order of a day or more, such an experiment is not possible. The long-lived, rapid scintillation of PKS 1257−326 makes it an ideal candidate for a time delay measurement, and in May 2002, the source was observed simultaneously with the VLA and the ATCA. This section presents the results of these observations. Another two sets of observations will be performed in early 2003, as repeated time delay measurements at different times of the year are expected to constrain the two-dimensional structure of the scintillation pattern.

6.3.2 The observations

The simultaneous ATCA and VLA observations took place on May 13 & 14, 2002. As PKS 1257−326 is setting at the VLA, which has an elevation limit of 8°, it rises at the ATCA, which has an elevation limit of 12°. The common visibility, as shown in Figure 6.4, lasts for 2.7 hours. The observations were performed at 6.2 and 3.5 cm to obtain two separate measurements of the time delay, and on two consecutive days (i) to increase the likelihood of seeing a deep minimum and maximum in the light curve on at least one day in order to tightly constrain the delay, and (ii) to determine how closely the delay repeated on consecutive days.

The VLA was split into two subarrays, each operating in the standard continuum

mode which consists of two contiguous 50 MHz channels, centred at 4.835 and 4.885 GHz for one subarray, and 8.435 and 8.485 GHz for the other. The observation was performed during VLA reconfiguration time, and not all antennas were available at all times. However, each VLA subarray always had > 10 antennas; more than double the collecting area of the ATCA, and the higher signal-to-noise of the VLA data is evident in Figures 6.5, 6.10 and 6.11. The full ATCA was used to observe simultaneously at 6.2 and 3.5 cm, with the same centre frequencies as the VLA, 4.86 and 8.46 GHz, respectively, and the standard 128 MHz continuum bandwidth. The edge channels of the ATCA data were discarded to match the frequency coverage of the VLA data.

The nearby secondary calibrator PKS 1255−316 was observed every 15 minutes for ~ 1 minute. This strong, > 2 Jy, unresolved calibrator shows no evidence of ISS at the observed frequencies, and is only $\sim 1^\circ$ away from PKS 1257−326 on the sky. Therefore PKS 1255−316 can be used to accurately correct for any elevation and time-dependent gain changes or pointing errors, assuming no significant systematic changes occur on a time-scale shorter than 15 minutes. Since the source was observed at low elevation at both telescopes, where the errors are largest, correcting for such effects is important.

6.3.3 Data reduction

The VLA data were loaded into AIPS for reduction, and the ATCA data into MIRIAD. 3C 286 was used as the primary calibration source at the VLA, and PKS 1934−638 at the ATCA. The accuracy of the primary calibration was not a major concern, as the flux density scales were subsequently adjusted so that the flux density of the secondary calibrator, PKS 1255−316, was identical in both datasets. However, it is interesting to note that the scaling factors applied to equalise the flux density of the calibrator were $< 2\%$ on both days at 4.9 GHz, and 4–6% at 8.5 GHz. Some of the discrepancy is due to the fact that 3C 286 is partly resolved at the VLA, which was not taken into account in the first-step calibration, since final antenna gain solutions were found using PKS 1255−316. Also, the primary calibrators were observed at different elevations and times from PKS 1255−316, which also introduces an error in the overall flux density calibration.

The complex gain solutions found using PKS 1255−316 were copied to PKS 1257−326. Figure 6.5 shows the 2002 May 14 data on PKS 1257−326 for each telescope, averaged over all baselines, where a time delay of order 8 minutes is clearly present. The significant difference in flux densities seen by each telescope is due to arcsecond scale structure in PKS 1257−326, which must be subtracted in order to accurately compare the flux density of the varying component observed at each telescope.

Subtraction of extended structure

The high sensitivity and good instantaneous (u, v) coverage of the VLA allowed high dynamic range images of PKS 1257−326 to be made, as shown in Figures 6.6 and 6.7. The images displayed were produced by J. E. J. Lovell, using the Difmap software package (Shepherd, 1997). The images at both frequencies show that the source has

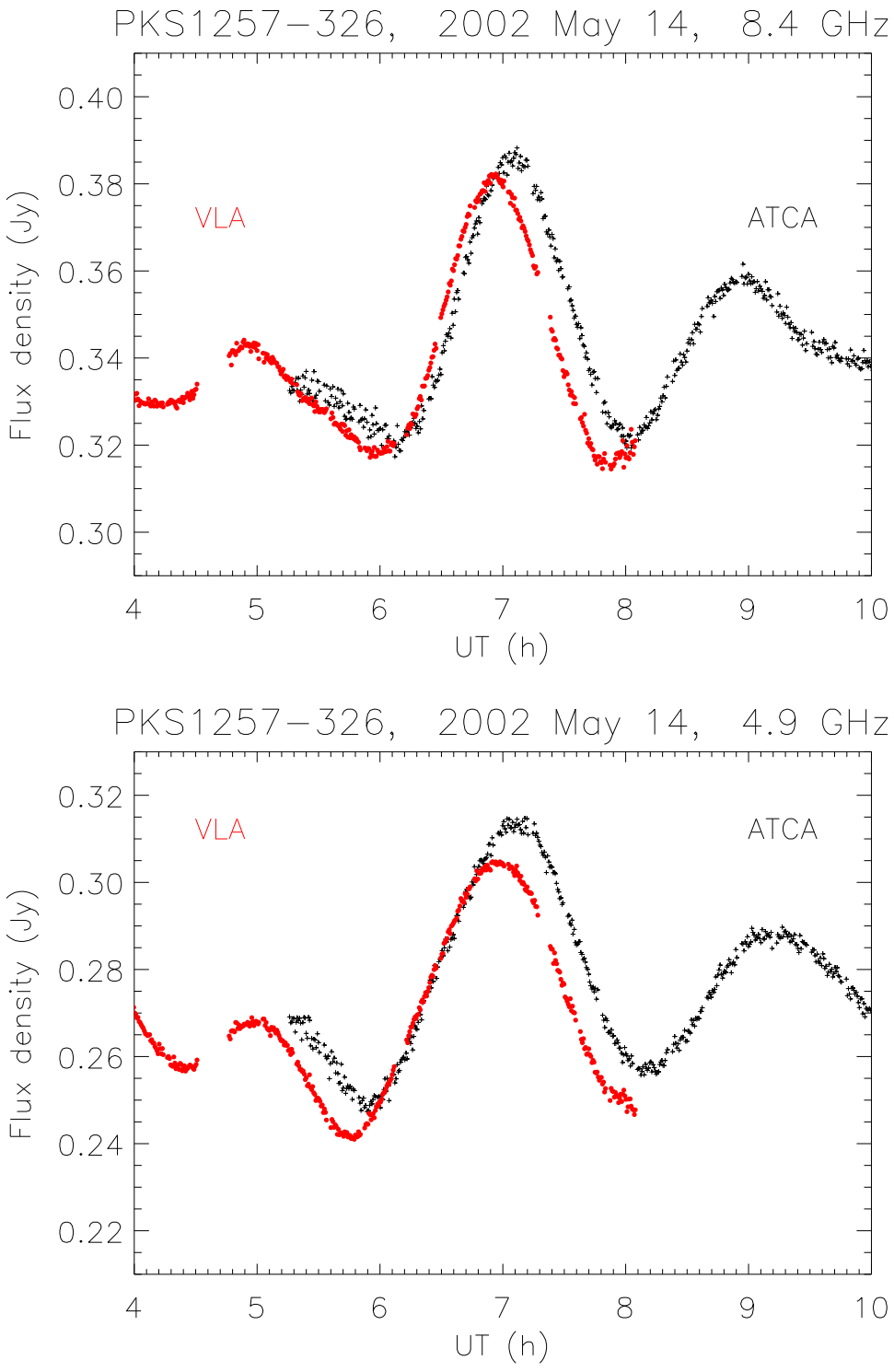

Figure 6.5: ATCA and VLA data from 2002 May 14 at 8.5 and 4.9 GHz, with the total flux density averaged over all baselines. The data have been calibrated using the nearby, unresolved source PKS 1255−316. The evident discrepancy in flux density is due to the arcsecond scale structure in PKS 1257−326, which is mostly resolved out on the long VLA baselines. See Section 6.3.3 for further discussion. Despite the vertical offset, a time delay of ~ 8 minutes is evident between the IDV patterns at each telescope.

a weak jet extending over a few arcseconds to the north-west. The corresponding model 'clean' components, except for the central strong point source which contains the scintillating component, were subtracted from both sets of visibilities in order to compare the ATCA and VLA flux densities in the May 2002 data. The subtraction was performed using AIPS task 'UVSUB'. The total flux densities outside the central point source component in the VLA images are 19 mJy at 4.8 GHz, and 9 mJy at 8.6 GHz.

Flux densities from the (u, v) data were then plotted to files using MIRIAD, with both 30-second and 1-minute averaging for comparison of results, and averaging over all baselines and frequency channels within each band. The VLA data are written with IAT (International Atomic Time) time coordinates, but these are decremented by 32 seconds to convert to UTC when read into MIRIAD, thus setting the time offset between the VLA and ATCA data to zero.

The resultant light curves, presented in Section 6.3.4, contain only the central source component which is unresolved at both telescopes, and any variation is due to scintillation rather than source structure. The effect of subtraction of the model extended components is illustrated in Figures 6.8 and 6.9. While the effect of structure is small compared to the scintillation, it is important to compare the flux densities at the two telescopes as accurately as possible, as this helps to constrain scintillation parameters. Depending on the scintillation length scale and direction of motion, each telescope may see a slightly different variability pattern.

6.3.4 Results and discussion

Figures 6.10 and 6.11 show the calibrated flux densities of the central component of PKS 1257−326, measured at both telescopes, at both frequencies and on both days. Immediately apparent is the close similarity of the patterns seen by each telescope, and the clear delay which is similar on both days and at both frequencies, with the VLA light curve leading.

The close to identical patterns at both telescopes imply that the pattern scale is much larger than the 10^4 km baseline, and the pattern can be assumed to be temporarily "frozen". The delay, which is $\sim$ 8 minutes on average, constrains the speed and direction of motion of the pattern. In fact there are a number of parameters contributing to the observed delay, and it is not possible to constrain them all independently. The fitting would be helped by repeated observations of the time delay at different times of the year, when the direction of $\mathbf{v}_{\rm ISS}$ is different. However, the consistency of the observed delay with the parameters found from the annual cycle in $t_{\rm ISS}$ may be tested. It is worth noting that for J1819+3845, the time delay observed between WRST and the VLA yielded quite a different ISM velocity from that originally estimated using the annual cycle in the characteristic time-scale (Dennett-Thorpe & de Bruyn, 2002, 2001).

For PKS 1257−326, the common VLA/ATCA visibility is much shorter than that for J1819+3845 as seen by the VLA and WSRT. Nevertheless, the projected baseline changes somewhat over this period, as shown in Figure 6.12. Note that this plot shows the baseline as seen looking down on Earth, the same projection as used in

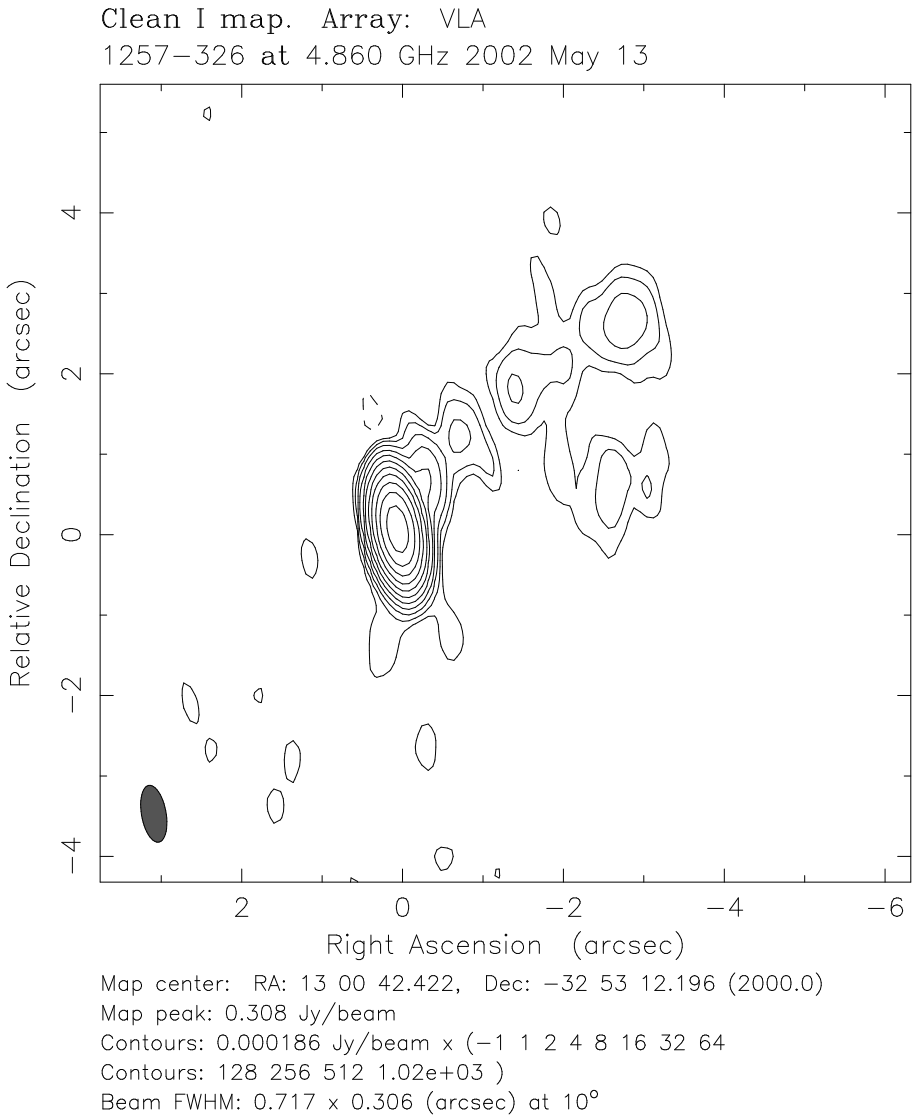

Figure 6.6: VLA image of PKS 1257−326 at 4.9 GHz (produced by J.E.J. Lovell). The corresponding 'clean' component model was used to remove the effect of extended structure from the visibilities in the data presented in Section 6.3.

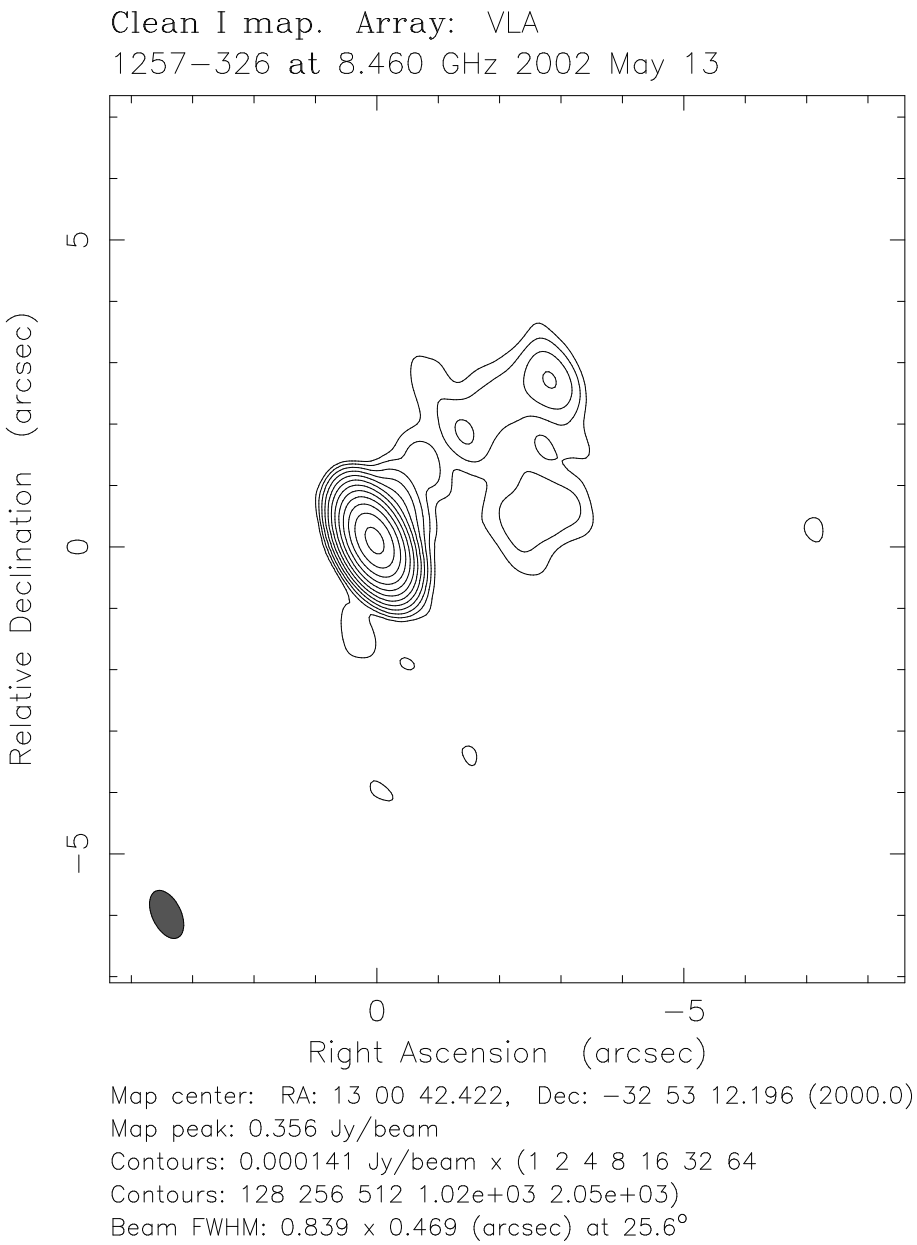

Figure 6.7: VLA image of PKS 1257−326 at 8.5 GHz (produced by J.E.J. Lovell).

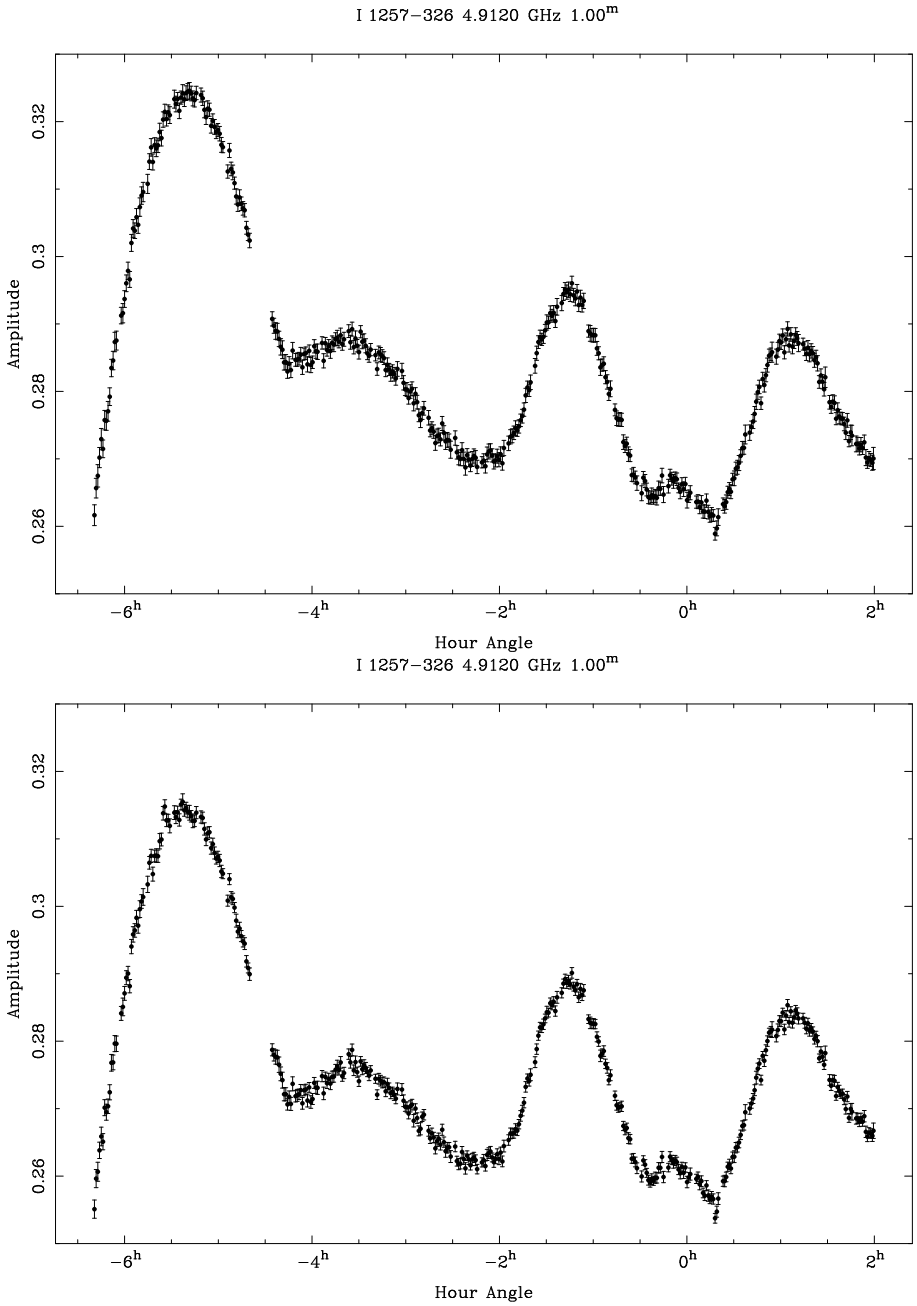

Figure 6.8: The effect of extended structure on ATCA visibilities for PKS 1257−326 at 4.9 GHz. Above: visibility amplitudes for Stokes I, averaged over all baselines before subtraction of extended components. Below: after subtraction of extended components.

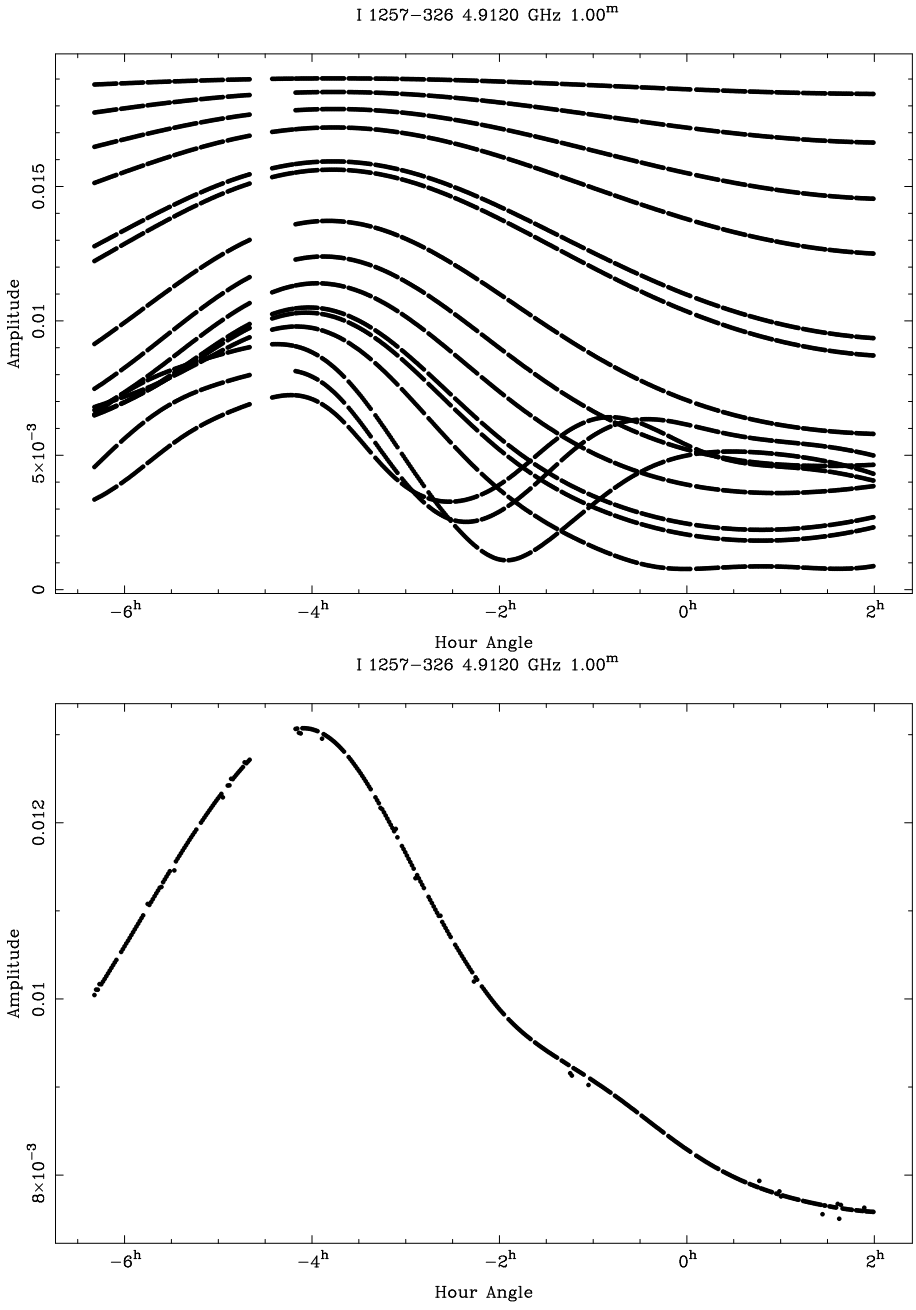

Figure 6.9: The difference between the visibility datasets displayed in Figure 6.8 above, corresponding to the extended component model visibilities. Above: visibility amplitudes plotted for each baseline separately. Below: visibility amplitudes averaged over all baselines, showing the overall effect of the extended structure on ATCA data. The effect is much smaller at 8.5 GHz. The gap near hour angle -4.5 is due to a failure of one of the ATCA antennas.

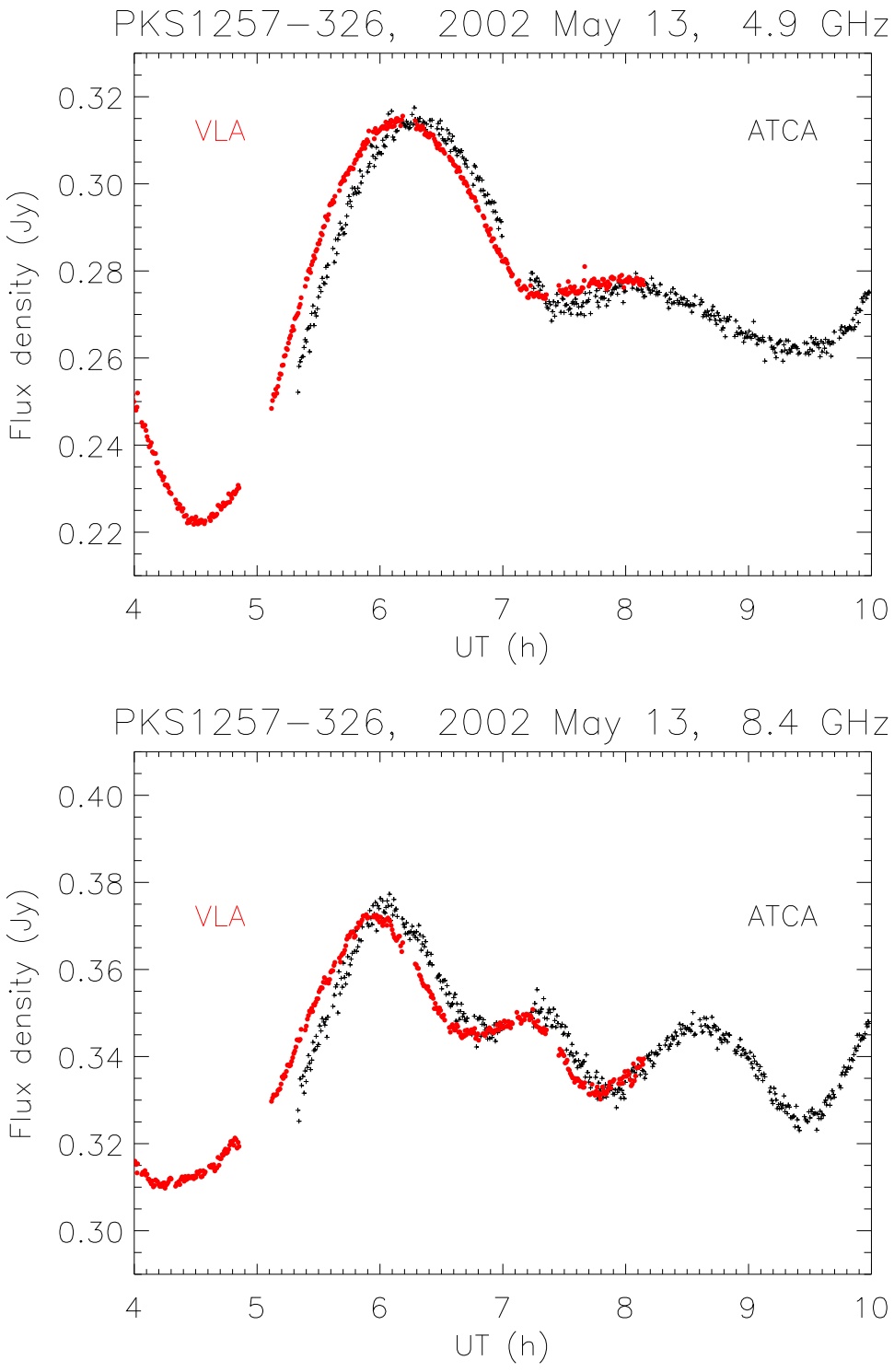

Figure 6.10: Simultaneous ATCA and VLA light curves for PKS 1257−326 on May 13, 2002, at 4.9 GHz (upper panel) and 8.5 GHz (lower panel). Flux density scales have been matched using the nearby, non-scintillating and unresolved source, PKS 1255−316. The contribution of extended components, modelled using the VLA data, has been subtracted from both sets of visibilities.

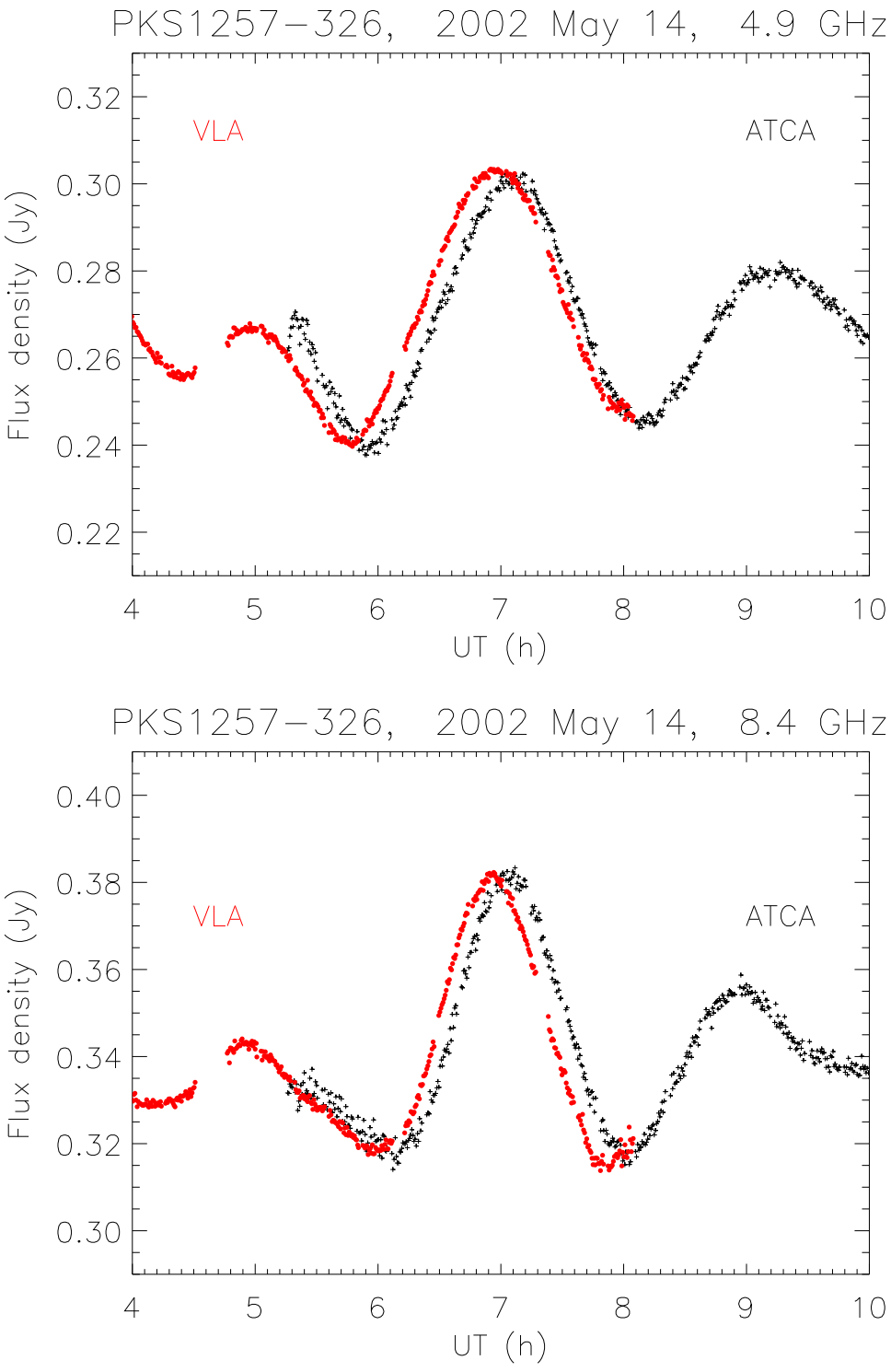

Figure 6.11: Simultaneous ATCA and VLA light curves for PKS 1257−326 on May 14, 2002, at 4.9 GHz (upper panel) and 8.5 GHz (lower panel). Flux density scales have been matched using the nearby, non-scintillating and unresolved source, PKS 1255−316. The contribution of extended components, modelled using the VLA data, has been subtracted from both sets of visibilities.

Figure 6.16*d*; (u, v) coverage is more often plotted with the opposite sign of u. The change in baseline vector $\mathbf{b}$ implies a change in pattern time delay is expected over the observation. However the delay is not entirely straight-forward to predict, as it depends not only on ISM velocity, but also on the angle at which the pattern crosses the baseline.

Recall that the scintillation pattern can be pictured as a series of bright and dark patches corresponding to regions of focusing and defocusing in the ISM. As described below in Section 6.5.1, there is evidence from the ATCA monitoring that this pattern is in fact highly elongated. Consider the case of an infinitely long, perfect sinudoidal variation, such as an idealised ocean wave. Then a peak or trough in the observed pattern could be considered to be a straight edge or wavefront which crosses both telescopes, with a delay depending on the distance the front has to travel in the perpendicular direction to cross both telescopes, and the component of its velocity in this direction.

Figure 6.12 illustrates this situation. In this figure, the projected baseline $\mathbf{b}$ at the beginning of the observation is shown by a dotted line, with the solid arc showing how $\mathbf{b}$ changes over the course of the observation. The dashed lines show the alignment of the anisotropy, assuming the pattern has a very large axial ratio. If this is the case, the pattern "front" travels a distance $b\cos(\xi)$ from, in this case, the VLA, to be seen at the ATCA, where ξ is the angle between the baseline and the "front" perpendicular. $\mathbf{v}_{\rm ISS}$ shows the direction of the ISM velocity with respect to the Earth on day of year 133, May 13, for a medium moving with the LSR. Then $v_{\rm perp}$ is the component of $\mathbf{v}_{\rm ISS}$ perpendicular to the front, and the time delay is $b\cos(\xi)/v_{\rm perp}$.

In reality, the scintillation pattern may be better modelled as a series of elliptical patches, and the angle at which a pattern "edge" crosses the telescopes may vary from one "scint" to the next. Coles & Kaufman (1978) analyse the general case for predicting the position of the peak of the temporal cross-correlation between intensities at two sites for any axial ratio, R, of the pattern. Since very few "scints" are sampled in the PKS 1257−326 observation, though, it is not possible to do a full statistical analysis as in, for example, the case of IPS studies described by Coles & Kaufman (1978). However, the fact that over two days, and at two frequencies, the delay observed is relatively constant, suggests that the simplified model of a highly elongated scintillation pattern may be appropriate. Repeated measurements of the time delay would be most useful to constrain the axial ratio of the scintillation pattern.

The same parameters are used to fit both frequencies and both days simultaneously. Fitting to the observed delay was performed using the model pictured in Figure 6.12, and varying v_α and v_δ, the components of $\mathbf{v}_{\rm ISS}$, and θ, which corresponds to the angle of the scintillation pattern *minor* axis, assuming a very large axial ratio. The best fits are found by minimising the sum of squares of the residuals, χ^2, when the predicted delay is subtracted from the data. The predicted delay changes by $< 20\%$ over the observation. The simultaneous fitting does not constrain all three parameters. Similar low values of χ^2 are found along a line in the $(v_\alpha, v_\delta, \theta)$ cube of parameter space. Although the fit is not unique, the best fit parameters from the annual cycle in characteristic time-scale, presented below in Section 6.5, coincide with a minimum χ^2 from the time delay at $v_\alpha = -44$ km s^{-1}, $v_\delta = 5.5$ km s^{-1}, and $\theta = 55°$. The predicted time

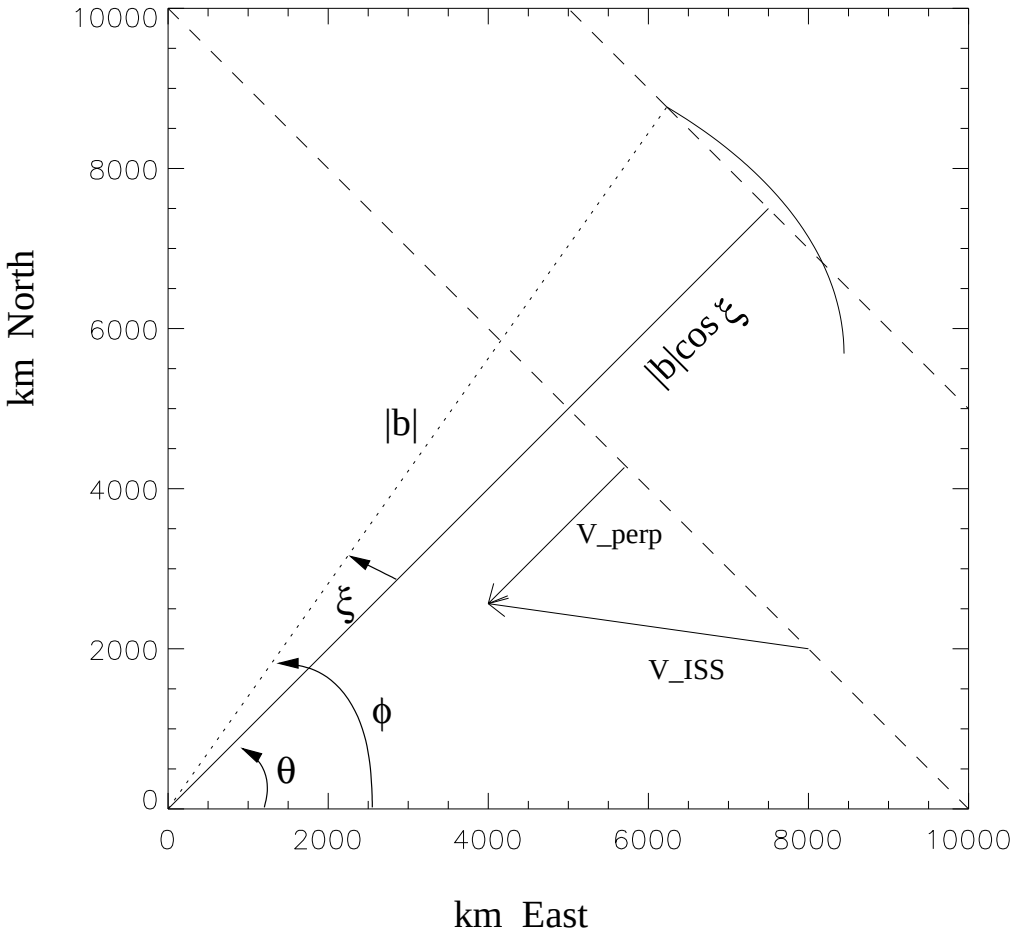

Figure 6.12: Parameters affecting two-station time delay. The dotted line of length $|b|$ represents the projected baseline in the (u, v) plane between the ATCA (at origin) and the VLA, at the beginning of the common visibility on PKS 1257−326. Note that this picture is drawn as if looking down on the Earth. The solid arc shows how the baseline changes over the observation. The parallel dashed lines represent the long axis of the scintillation pattern. The arrow $V_{\rm perp}$ represents the component of the scintillation velocity $V_{\rm ISS}$, in the direction perpendicular to the long axis of the pattern. $V_{\rm ISS}$ is the direction of the ISM velocity with respect to the Earth for the 2002 May observations. The arrow shown here is for a medium moving with the local standard of rest (LSR). In fitting to the data, the free parameters were the angle θ, corresponding to the direction of the short axis of the scintillation pattern, and the two components of $V_{\rm ISS}$ in the plane of the sky.

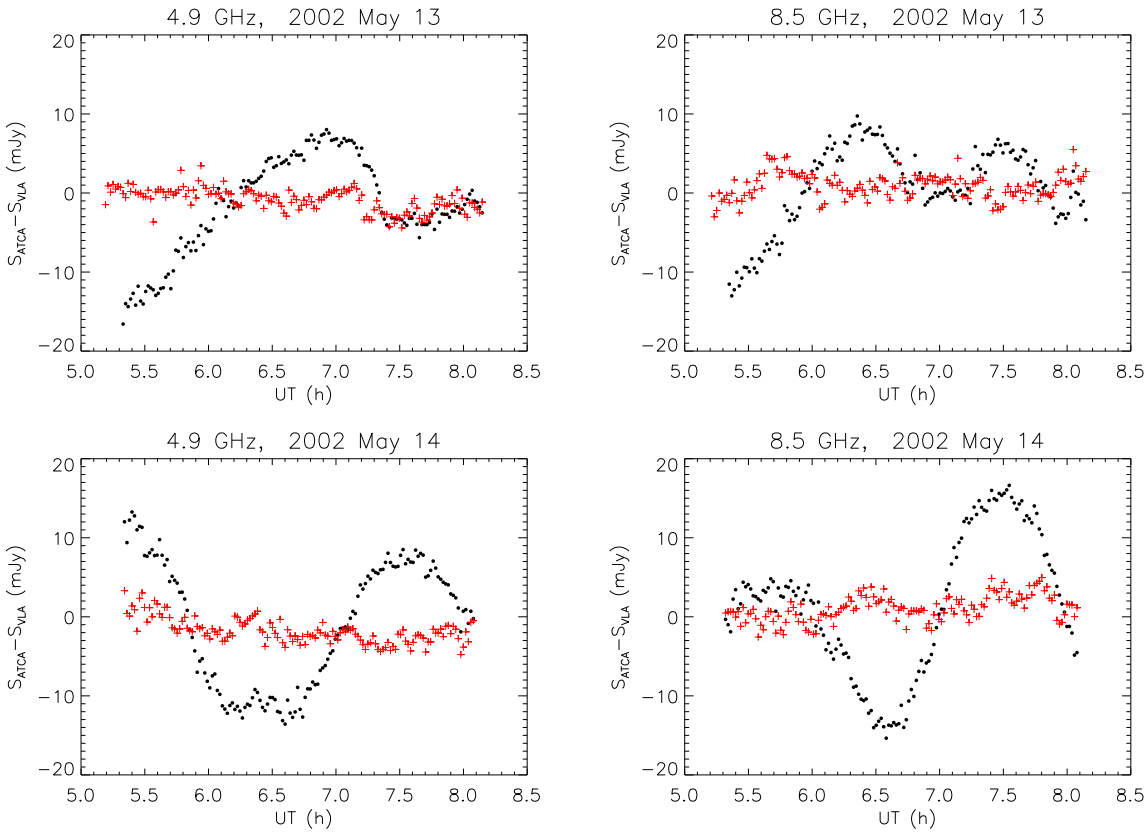

Figure 6.13: Flux density difference between the calibrated VLA and ATCA datasets, with no delay correction (black dots), and after correcting for the predicted delay (red + symbols), for $v_\alpha = -44$ km s^{-1}, $v_\delta = 5.5$ km s^{-1}, and $\theta = 55°$, assuming a highly anisotropic scintillation pattern (see Section 6.3.4 for explanation).

delay then varies from 8.7 to 7.6 minutes over the course of the observation, with the VLA leading. Figure 6.13 shows the residual flux densities before and after applying the delay correction. The variation of the delay over the course of the observation is almost insignificant, quite unlike the VLA/Westerbork observations of J1819+3845, where the delay was observed to change direction over the course of the observation. For PKS 1257−326, the proposed observations to measure the delay at different times of the year are important to constrain the scintillation parameters.

The similarity of the displaced variability patterns observed at the VLA and ATCA shows unequivocally that the rapid variability in PKS 1257−326 is dominated by interstellar scintillation. Furthermore, the delay of several minutes over a 10^4 km baseline implies that the ISM moves with a velocity of the same order of magnitude as the Earth's orbital velocity, 30 km s^{-1}. In this case, one would expect to see an *annual cycle* in the characteristic time-scale of variability, due to the changing velocity of the Earth relative to the ISM. The next section presents results of over a year's monitoring of PKS 1257−326 with the ATCA.

6.4 Results of ATCA monitoring of PKS 1257−326

6.4.1 Annual cycle in the characteristic time-scale

Figure 6.14 presents nine of the light curves at 4.8 and 8.6 GHz made at approximately six week intervals over 12 months, as part of the C927 program (Chapter 5). Immediately apparent is the dramatic change, over the course of the observations, in the time-scale of the flux density variations at both frequencies. From February through May, the flux density varies rapidly with less than one hour between excursions. In June the variations begin a slow down which lasts through September. November sees them speed up again, while by 2002 January they have returned to much the same rate as 2001 February. The time-scales estimated from the earlier discovery observations of 2000 June and September, and the more recent observations of 2002 February and April, are consistent with this *annual cycle* in the time-scale of variations. The annual cycle provides clear evidence that the observed rapid variations are due to interstellar scintillation (ISS). The change in the time-scale of variations through the year is due to the changing velocity of the scattering medium relative to the observer as the Earth revolves around the sun.

The effect of unsubtracted source structure (Section 6.3.3) does not affect any of the results presented in this chapter. Subtraction of the extended components has not yet been performed for most of the ATCA data, apart from that presented in Section 6.3. The contribution from extended structure is different on different baselines, and the effect tends to be "smoothed out" by averaging over all baselines. At 4.8 GHz, unsubtracted extended components cause an additional, spurious "variation" of ~ 5 mJy peak-to-peak. At 8.6 GHz, the peak-to-peak variation due to extended structure is ~ 2 mJy. The effect of the extended structure on the visibilities is, however, small compared to the rapid, large amplitude variability displayed by PKS 1257−326. The observed peak-to-peak variation in flux density is several tens of mJy at both frequencies.

The data displayed in Figures 6.14 are averaged over 1 minute and over all baselines. The thermal noise for 1-minute integrations is ~ 1 mJy, neglible compared with the observed variations. Peak-to-peak proportional errors in these data (see Section 2.3.5), are typically $\sim 1\%$ at 4.8 GHz, and $\sim 2\%$ at 8.6 GHz. Some data, including that presented in Section 6.3, have been calibrated using the nearby source PKS 1255−316, which is unresolved at both frequencies at a level $\gg 99\%$. Observations of PKS 1255−316 allow correction for most errors due to pointing, gain-elevation, and opacity effects, in which case the amplitude calibration is estimated to be accurate to better than 0.5%.

To quantify the observed changes, the characteristic time-scale of variability is defined as the half-width at half-maximum of the auto-correlation function (ACF), $t_{0.5}$. The ACFs calculated at each frequency for the data of 2001 March 23 are shown in Figure 6.15 as an example. Figures 6.16*a* and 6.16*b* show $t_{0.5}$, determined for each session and at both frequencies, plotted against day of year. This shows quantitatively the remarkable annual cycle so apparent in Figure 6.14. Also included are the $t_{0.5}$ values calculated for the data from 2000, and the more recent observations of 2002 February

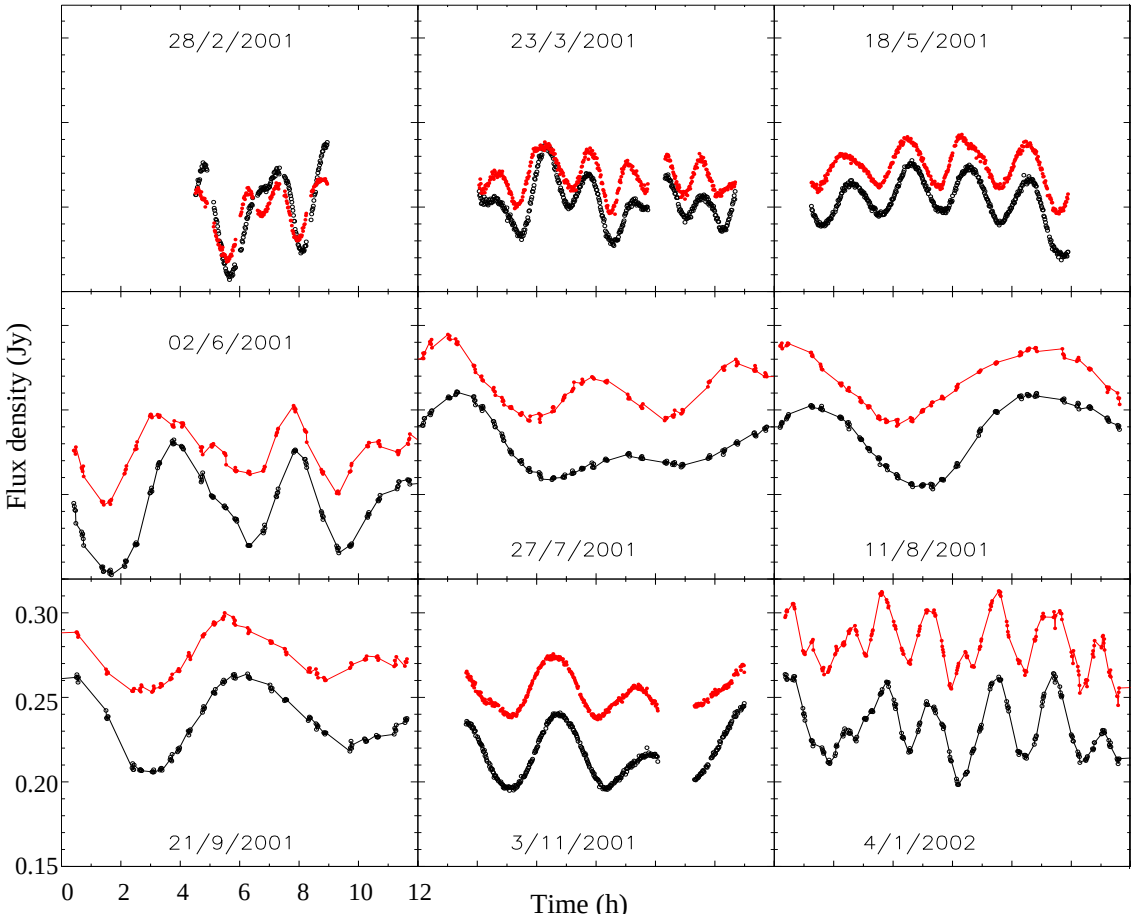

Figure 6.14: Light curves over the course of a year for PKS 1257−326. All plots are on the same scales, shown on bottom left plot. 4.8 GHz data are represented by black circles; 8.6 GHz data are represented by filled red circles.

and April. The values for 2000 are plotted as limits. As shown in Figure 6.2, the light curve from June 2000 was somewhat undersampled and therefore gives an upper limit to $t_{0.5}$, while the 2000 September data showed a decrease in flux density over 4 hours, with a subsequent 4.5 hour gap in the data (due to observations for another project) followed by an increase over the next 3 hours, so we have only a lower limit on $t_{0.5}$. Plotted in Figure 6.16*c* is the expected scintillation speed *vs* day of year, assuming that the ISM is moving with the local standard of rest (LSR) (Rickett et al., 2001, and private communication). Figure 6.16*d* displays the corresponding scintillation velocity projected onto the plane transverse to the source line-of-sight. Comparison of the time-scale with the scintillation speed shown in Figure 6.16 demonstrates that the phasing of the annual cycle is close to, but does not exactly match, the Earth's projected speed with respect to the LSR. The annual cycle in $t_{0.5}$ is a result of the changing velocity of the scintillation pattern across the observer's line-of-sight, and leaves no doubt as to the origin of the intra-day variability in this source. Such an annual cycle has been seen in two other sources; 0917+624 (Rickett et al., 2001; Jauncey & Macquart, 2001), and J1819+3845 (Dennett-Thorpe & de Bruyn, 2001). This is expected if the IDV is in fact a propagation effect caused by a relatively local Galactic "screen". To reflect the ISS nature of the rapid variations, the characteristic time-scale, estimated as the 50% decay time of the ACF, is hereafter referred to as $t_{\rm ISS}$.

Estimating the error in $t_{\rm ISS}$

Scintillation is a stochastic process, and since the observations sample this process over a finite duration, it is only possible to obtain an approximation to the true time-scale of the underlying process. The limited sampling of a stochastic process is by far the dominant contribution to the uncertainty in any determination of the scintillation time-scale, $t_{\rm ISS}$. The uncertainty decreases with the number of independent samples of the scintillation pattern, or "scints", observed.

To estimate the error empirically, the datasets from 12 well-sampled epochs, when $t_{\rm ISS}$ is short and/or the dataset extends over two consecutive days, were divided into subsets, and $t_{\rm ISS}$ was calculated for each subset. It is assumed that the statistical error due to the finite number of samples of the stochastic process scales as $1/\sqrt{N}$, where N is the number of independent samples. N in this case is defined as $T_{\rm obs}/t_{\rm ISS}$, where $T_{\rm obs}$ is the length of the observation. It is then assumed that the fractional error, $\sigma_t/t_{\rm ISS}$, is proportional to $\sqrt{t_{\rm ISS}/T_{\rm obs}}$. For each subset, $E_t = \sqrt{2}[t_{\rm ISS}(\text{full dataset}) - t_{\rm ISS}(\text{subset})]$ is calculated, where the $\sqrt{2}$ arises because the two estimates are not independent. From the observed distribution of $E_t\sqrt{N}/t_{\rm ISS}$, the 1σ fractional errors are estimated to be $\sigma_t/t_{\rm ISS} = 0.7\sqrt{t_{\rm ISS}/T_{\rm obs}}$ at 4.8 GHz, and $\sigma_t/t_{\rm ISS} = 0.9\sqrt{t_{\rm ISS}/T_{\rm obs}}$ at 8.6 GHz. The resultant error bars are shown in Figure 6.16.

To evaluate the reliability of the above error estimates, it is assumed that $t_{\rm ISS}$ is constant between day of year 50 and day of year 150 (late February through May), an assumption supported by the data in Figure 6.16, and by the almost constant value of $v_{\rm ISS}$ (for a medium moving with the LSR, as shown in Figure 6.16*c*) over this period. The observed rms scatter in the 8 data points from this period is 12% at 4.8 GHz and

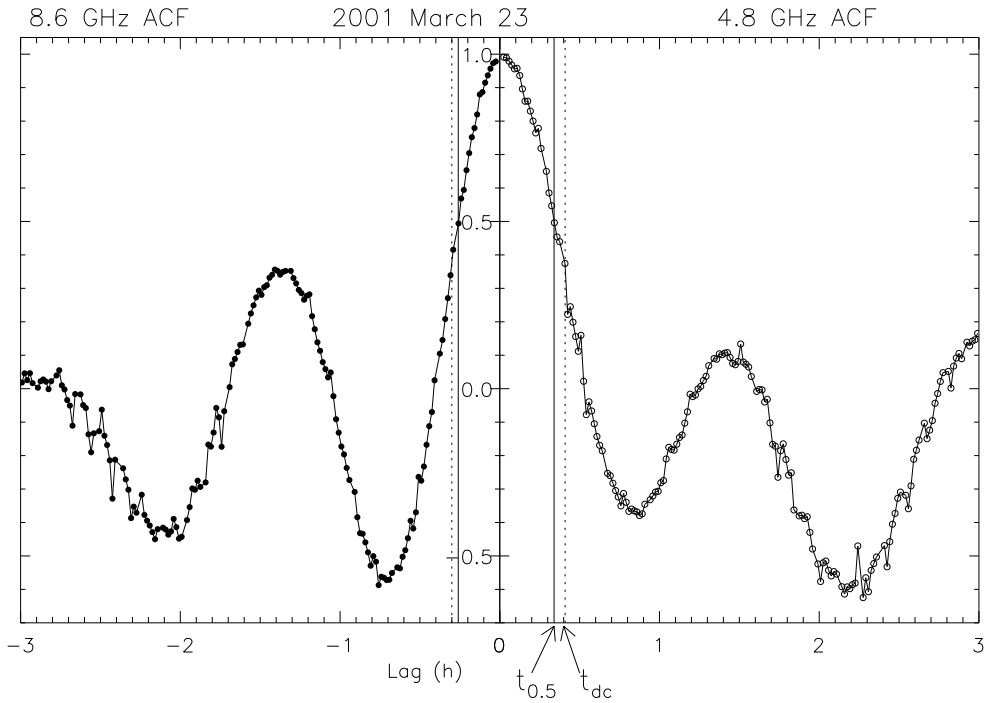

Figure 6.15: Auto-correlation functions for data from 2001 March 23, at 8.6 GHz (filled circles) and 4.8 GHz (open circles). The characteristic time-scale is defined here as the half-width at half-maximum of the ACF, $t_{0.5}$, which is indicated in the Figure. The half-width at $1/e$, or "de-correlation time-scale", $t_{\rm dc}$, is also shown - some authors define the characteristic time-scale to be $t_{\rm dc}$ (e.g. Cordes, 1986; Macquart & Jauncey, 2002).

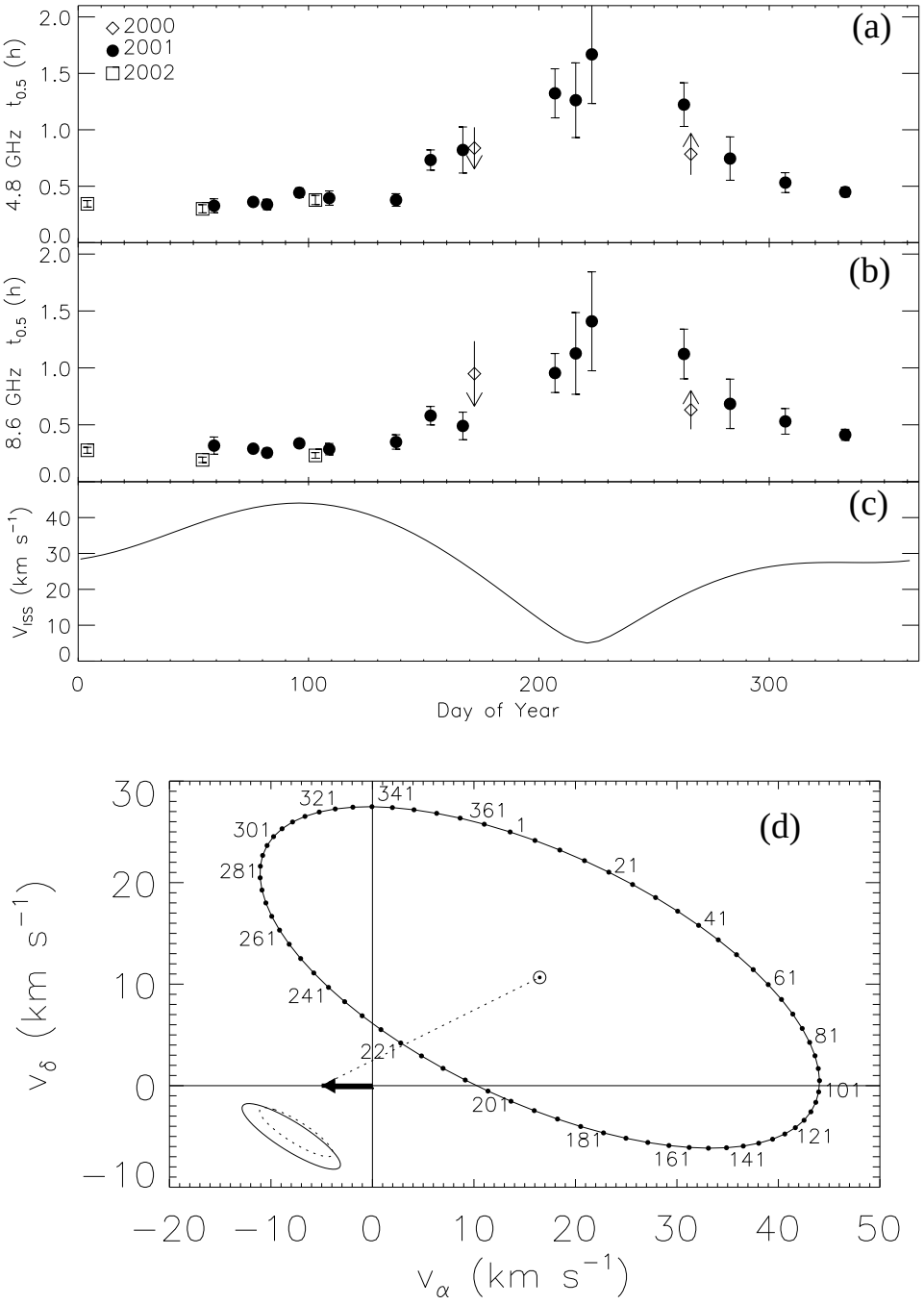

Figure 6.16: Characteristic timescale $t_{0.5}$ (defined as the HWHM of the ACF) *vs* day of year at (a) 4.8 GHz and (b) 8.6 GHz. Values for 2000 are limits (see Section 6.4.1 for details). (c) Expected scintillation speed v_{ISS} *vs* day of year for a scattering medium moving with the LSR. (d) The corresponding scintillation velocity $\mathbf{v}_{ISS}$ projected onto the plane transverse to the source line-of-sight, in components of RA (v_α) and Dec (v_δ). Arrow shows offset velocity of $(\delta v_\alpha, \delta v_\delta) = (-5, 0)\,\mathrm{km\,s^{-1}}$. Small solid ellipse shows a contour of the best fit scintillation pattern at 4.8 GHz, while dotted ellipse shows contour at 8.6 GHz, with the corresponding offset estimated in Section 6.5.7 plotted on the same scale.

19% at 8.6 GHz, compared with the mean of the errors determined for these data as above, of 13% at 4.8 GHz and 15% at 8.6 GHz. This indicates that the error estimates, as derived above, are reasonable.

6.4.2 Long term trends

The increasing difference between the mean flux density levels in Figure 6.14 reveals that the spectral index became increasingly inverted as the mean flux density at 8.6 GHz increased by 70%, while that at 4.8 GHz increased by 35%. This is clearly seen in Figure 6.17, which shows all data from well-sampled epochs at both frequencies, as well as the mean spectral index at each epoch. The source appears to be undergoing a pc-scale "outburst" of the type commonly seen in many flat-spectrum AGN (e.g., Kellermann & Pauliny-Toth, 1968). Figure 6.17 also shows that despite the increase in total flux density, there has been no dramatic increase or decrease of the rms variations at either frequency. Regression analysis (see Figure 6.18) shows evidence for a slight increase with time in the rms variations at 8.6 GHz. The correlation coefficient, assuming a linear increase with time at 8.6 GHz, has a value of 0.48, although there is substantial scatter in the data. In comparison, there is no significant change in the rms flux density variations at 4.8 GHz; the correlation coefficient for the regression is only 0.08. Monitoring of PKS 1257−326 is ongoing, in order to investigate the connection between ISS and intrinsic source changes. This connection is further discussed in Section 6.6.

6.4.3 Time offset between 4.8 and 8.6 GHz scintillation patterns

Close inspection of Figure 6.14 reveals that at each epoch, the 8.6 GHz variability pattern appears to lead the 4.8 GHz light-curve. The time delay between the variations at the two frequencies, $\tau_{(4.8,8.6)}$, was quantified by cross-correlating the 4.8 and 8.6 GHz observations at each epoch. Although the overall variability patterns at both frequencies are quite similar, there is some extra "structure" in the 8.6 GHz light curves which appears to be more smoothed in the 4.8 GHz light curves. Therefore only light curves with well-sampled peaks and troughs give a reliable time delay measurement. As shown in Figure 6.19, the peak of the cross-correlation always has the same sign, i.e. the 8.6 GHz variations are leading. Although the uncertainty in each individual measurement is large, due to limited sampling and the fact that the light curves at each frequency are not identical, this result is significant. Interestingly, there is a clear correlation of $\tau_{(4.8,8.6)}$ with the inverse of the predicted ISM velocity (Figure 6.16), indicating another annual cycle in the scintillation pattern of this source. In the next section, the implications of these results for PKS 1257−326 and the ISM in the line-of-sight to this source are examined in detail.

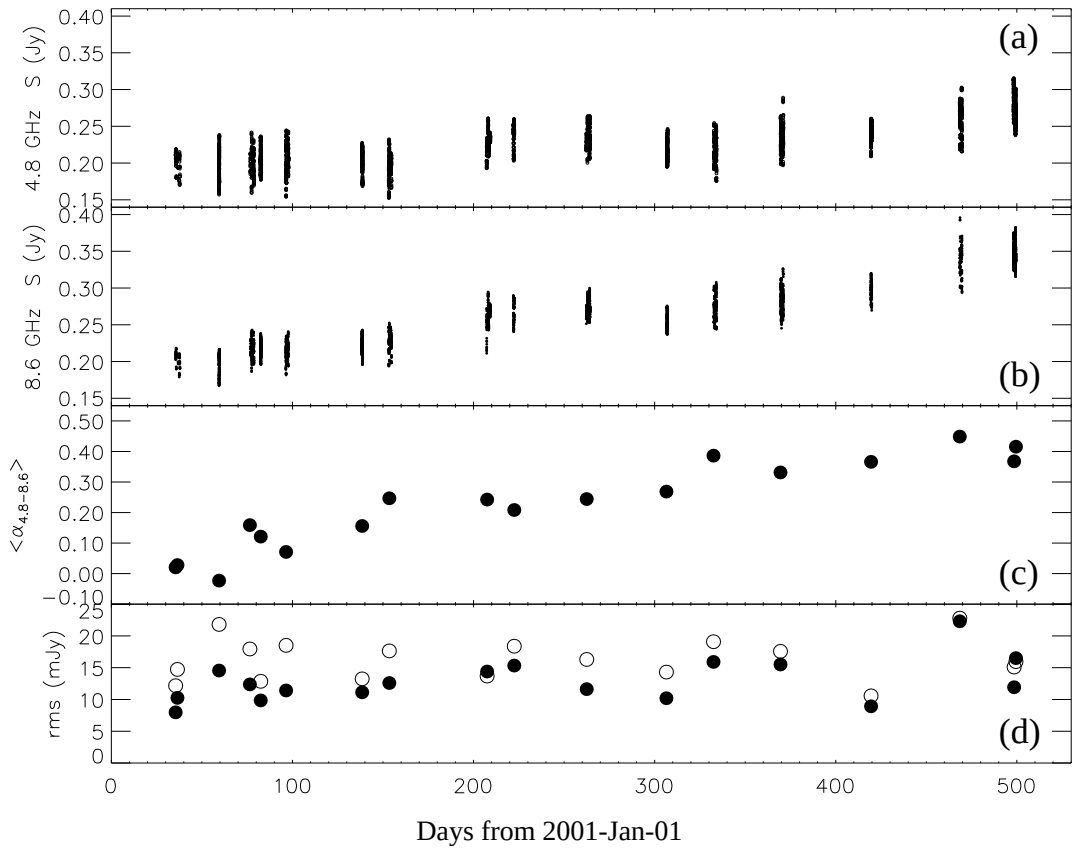

Figure 6.17: Flux density at (a) 4.8 and (b) 8.6 GHz, from all well-sampled epochs, plotted with 1-minute averaging. (c) Mean spectral index from each epoch. (d) rms variation for each epoch at 4.8 GHz (open circles) and 8.6 GHz (closed circles).

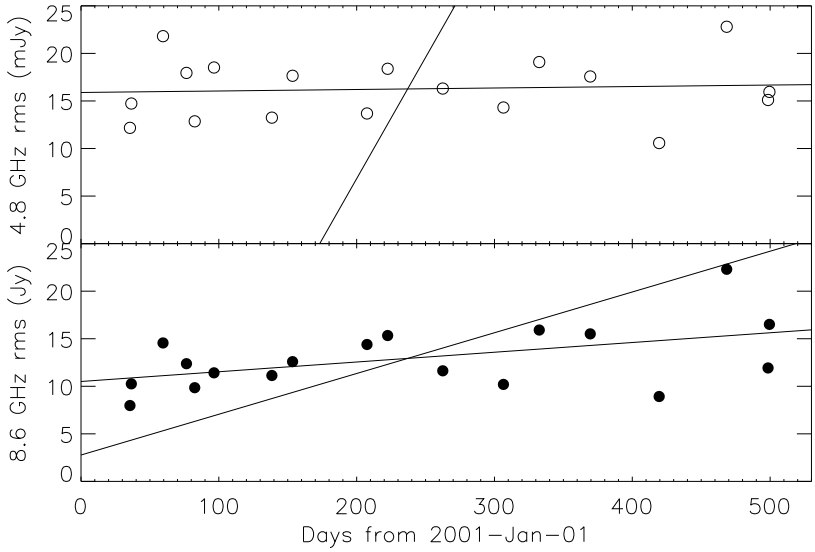

Figure 6.18: Regression lines for a linear change in rms flux density variations with time. No trend is observed for the rms variations at 4.8 GHz (correlation coefficient 0.08), while at 8.6 GHz there is evidence for a slight increase with time in the flux density of the scintillating component (correlation coefficient is 0.48). See Section 6.4.2 for discussion.

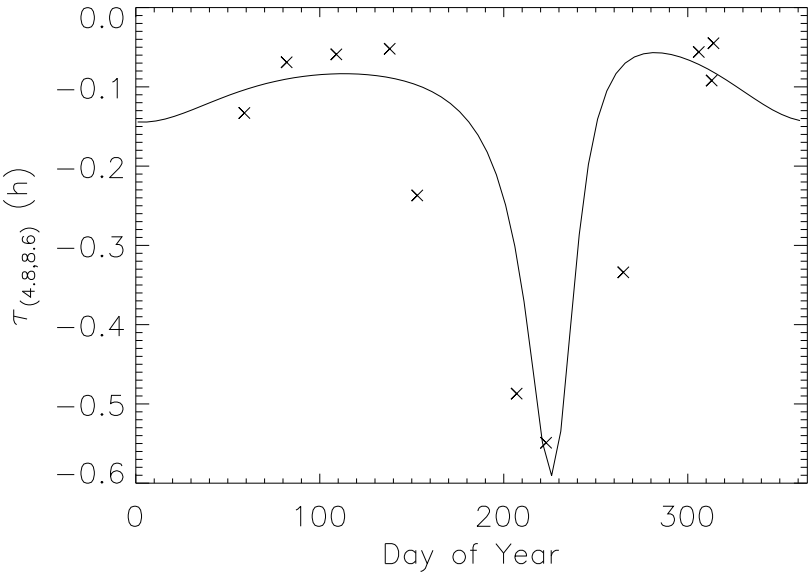

Figure 6.19: The time offset between 8.6 and 4.8 GHz light-curves. Line shows expected annual cycle for a fixed offset between the centroids of the two components (see Section 6.5.7).

6.5 Modelling the annual cycle & microarcsecond source structure

The clear presence of an annual cycle in the characteristic time-scale of variability identifies interstellar scintillation as the mechanism responsible for the IDV in PKS 1257−326, which in turn allows a determination of both source and scattering screen properties. Over the course of a year, the Earth's orbital motion produces changes in both the magnitude and direction of the scintillation velocity, $\mathbf{v}_{\rm ISS}$, which both potentially contribute to changes in $t_{\rm ISS}$. Figure 6.16*d* shows the Earth's velocity relative to the LSR over the course of a year, projected onto the plane transverse to the source line-of-sight. If the scintillation pattern is isotropic, only the change in the scintillation *speed* contributes to variations in $t_{\rm ISS}$. In this case, the observed $t_{\rm ISS}$ is inversely proportional to $|\mathbf{v}_{\rm ISS}|$. However, the length scale of the scintillation pattern may change with orientation, in which case $t_{\rm ISS}$ will also change as the *direction* of $\mathbf{v}_{\rm ISS}$ changes. An elongated scintillation pattern could be produced by elongated source structure and/or by anisotropic scattering in the ISM.

6.5.1 Anisotropic scattering

Rickett et al. (2002) showed that the deep first minimum, which they term a negative "overshoot", in the ACFs for data on PKS 0405−385 during its episode of fast scintillation, indicates that the scattering is highly anisotropic. Their results from numerical simulation suggest that the scintillation pattern of PKS 0405−385 has an axial ratio of 0.25 or less, where $\mathbf{v}_{\rm ISS}$ is approximately aligned with the short axis of the irregularities. For more highly anisotropic irregularities, the depth of the ACF first minimum does not change significantly. The negative overshoot is a measure of the spectral purity of the fluctuations: the closer to sinusoidal the variations are, the closer to -1 is the depth of the first minimum in the ACF. Rickett et al. (2002) argue that the negative overshoot is an effect of anisotropic scattering in the ISM, and cannot be duplicated by anisotropic source structure.

A large number of independent samples of the scintillation pattern are required to determine a reliable ACF. For light curves which sample only 1 or 2 scintels, the ACF is poorly determined and thus a spurious negative overshoot can occur. For all of the long datasets on PKS 1257−326, the average depths of the first minima in the normalized ACFs are (-0.5 ± 0.1) and (-0.3 ± 0.1), at 4.8 GHz and 8.6 GHz respectively. Assuming that the model of Rickett et al. (2002) applies to PKS 1257−326, this indicates that the scattering is anisotropic, with the *minor* axis of the scintillation pattern aligned within $\sim 45^\circ$ of the plasma velocity vector. The minima at 4.8 GHz are, on average, deeper than at 8.6 GHz, although there is substantial scatter (for example, Figure 6.15 shows that for the 2001 March 23 data, the first minimum of the ACF was in fact deeper at 8.6 GHz.) The fact that the average size of the "negative overshoot" differs at each frequency may be a result of a differing source size relative to the Fresnel scale, i.e. the 8.6 GHz component may have a larger ratio of angular source size to angular

size of the first Fresnel zone, $\theta_S : \theta_F$, than the 4.8 GHz component. Hence the negative overshoot in the ACF could be suppressed at 8.6 GHz as source size effects become more important.

6.5.2 Scintillation length scales

The large amplitude of the variations at 4.8 and 8.6 GHz, and strong similarity of the scintillation patterns at the two frequencies, indicate that 4.8 and 8.6 GHz are slightly above the transition frequency in the regime of weak scattering, where the medium introduces a phase change of less than 1 radian across a Fresnel zone. Broadband variability across this frequency range is a pattern commonly seen in other IDV sources at high Galactic latitudes, in particular the other extreme IDVs. At lower frequencies, t_{ISS} is generally much longer and the variability is not correlated with the higher frequency variability. This is explained in terms of weak and strong scattering. At 4.8 and 8.6 GHz, the sources undergo weak scintillations, while lower frequencies (below $\sim$ 3 GHz) are in the regime of strong (refractive) scattering (e.g. Kedziora-Chudczer et al., 1997; Walker, 1998). Time-scales of variability for strong, refractive scintillations increase with wavelength, λ, as $\lambda^{11/5}$.

In the regime of weak scattering, the typical length scale of the scintillations is equal to the Fresnel scale, $r_F = \sqrt{cL/(2\pi\nu)}$, where L is the distance to the scattering plasma and ν is the observing frequency. The Fresnel scale sets an effective cut-off diameter for the angular size of a source undergoing weak scintillation, $\theta_F = r_F/L$. A source this size or smaller exhibits flux density variations on a time-scale $t_{ISS} = r_F/v_{ISS}$, where v_{ISS} is the speed of the scattering material across the line of sight. For larger source sizes, $\theta_S > \theta_F$, the scintillations decrease in amplitude as $1/\theta_S$ and increase in timescale as θ_S (e.g. Rickett, 2002). It may be that AGN have a sufficiently large angular diameter that the source size influences the observed scintillation pattern. Another effect of larger source sizes is that scintillations from distant scattering material are suppressed, since the angular size "cut-off", set by the first Fresnel zone, scales as $1/\sqrt{L}$. Therefore, there will be a bias towards finding sources that scintillate behind ISM turbulence which is close to the solar system.

The measurements of the annual cycle in t_{ISS} can be used to constrain (i) the velocity of the scattering medium, $\mathbf{v}_{ISM}$, which Figure 6.16 suggests is not very different from the LSR, (ii) the source angular size, θ_S, and (iii) the distance to the scattering screen, L. The parameters used to model the observed annual cycle in t_{ISS} are as follows. $\mathbf{v}_{ISM}$ may be offset from the LSR and this introduces two free parameters, the components of this offset in the plane transverse to the source line-of-sight. As illustrated in Figure 6.16*d*, the projected velocity of the sun with respect to the LSR in RA and Dec components is $v_\alpha = 16.5$ km s^{-1}, $v_\delta = 10.7$ km s^{-1}. The RA and Dec offsets, δv_α and δv_δ, of the $\mathbf{v}_{ISM}$ components shift the origin in Figure 6.16*d*. Two more parameters are required to describe the axial ratio and orientation of anisotropy in the scintillation pattern. Finally there is an overall scaling factor, s_0, which sets the scintillation length scale. s_0 is chosen to be the minor axis of the scintillation pattern. The shape of the resulting annual cycle is quite sensitive to variations in the ISM velocity and the angle of the

elongation for an anisotropic scintillation pattern.

The best fit parameters at each frequency are found by minimising the sum of squares of the residuals. Fits have been found both for the case of unweighted residuals, and for the case of residuals weighted by the error associated with each point. The shape of the slow-down period is critical in determining the ISM velocity and anisotropy in the scintillation pattern. However the errors in $t_{\rm ISS}$ are larger in this period, due to having fewer independent samples of the scintillation pattern. Using the unweighted residuals (i.e. ignoring the errors), the fit is better constrained by these points in the slow-down period. On the other hand, the overall scintillation length-scale is more accurately estimated using the better-sampled data from the fast period. For the models which fit well to the data, using weighted or unweighted residuals makes little difference to the results.

6.5.3 The isotropic case

For simplicity, the case of isotropic scattering and an isotropic source is first considered in fitting to the annual cycle. While there is strong evidence, from the observed two-station time delay (see Section 6.3) and the autocorrelation functions, for anisotropy in the scintillation pattern, fitting to both anisotropy *and* ISM velocity involves five free parameters. The case of an anisotropic scintillation pattern is considered later, and as discussed below, the constraints on source size and screen distance allowing an anisotropic pattern are not significantly different from the isotropic case. In the isotropic case, the best fit to the peak in $t_{\rm ISS}$ is achieved with $\delta {\rm v}_\alpha = -7$ km s^{-1} and $\delta {\rm v}_\delta = -2$ km s^{-1} at 4.8 GHz. At 8.6 GHz the best fit is for $\delta {\rm v}_\alpha = -7$ km s^{-1} and $\delta {\rm v}_\delta = +2$ km s^{-1}. Assuming the same scattering material is responsible for the scintillation at both frequencies, the average is taken as the overall best fit: $\delta {\rm v}_\alpha = -7$ km s^{-1} and $\delta {\rm v}_\delta = 0$. These fits, and fits for several other velocity offsets, are shown in Figure 6.20. The scintillation length-scale, s_0, is a function of L and $\theta_{\rm S}$. While it is likely that source size influences the scintillation in PKS 1257−326, the size of the scintillating component, $\theta_{\rm S}$, cannot be very much larger than the Fresnel scale, otherwise the source would not show such deep modulations in flux density. Introducing a scaling parameter

$$R_\theta = \begin{cases} 1 & \text{if } \theta_{\rm S} < \theta_{\rm F} \\ \theta_{\rm S}/\theta_{\rm F} & \text{otherwise} \end{cases} \tag{6.1}$$

and approximating the scintillation length scale as $s_0 \approx L\theta_{\rm S} \approx R_\theta r_{\rm F} = R_\theta \sqrt{cL/2\pi\nu}$, the screen distance can be estimated as

$$L \approx 0.068 \left(\frac{1}{R_\theta^2}\right) \left(\frac{s_0}{10^4 \text{ km}}\right)^2 \left(\frac{\nu}{1\,\text{GHz}}\right) \text{ pc} \tag{6.2}$$

Because $L \propto s_0^2$, uncertainties in s_0 lead to greater uncertainties in L, and the screen distance is rather weakly constrained. For the isotropic case, the allowable range of values found for the scintillation length-scale are $s_0 = 6 \pm 1 \times 10^4$ km at 4.8 GHz, and $s_0 = 5 \pm 1 \times 10^4$ km at 8.6 GHz. Letting $R_\theta = 1$ (i.e. $s_0 = r_{\rm F}$) gives an approximate upper

limit on L. Inserting these values gives $L \approx 12 \pm 4$ pc at 4.8 GHz, and $L \approx 15 \pm 6$ pc at 8.6 GHz. This implies that the scattering occurs in a very local region of turbulence, as has been suggested for the other two intra-hour scintillators, J1819+3845 (Dennett-Thorpe & de Bruyn, 2000) and PKS 0405−385 (Rickett et al., 2002). If $R_\theta > 1$, this implies an even closer screen. For a distance in the range 10–15 pc, $r_{\rm F}$ corresponds to an angular size in the range 30–37 μas at 4.8 GHz, and 22–28 μas at 8.6 GHz.

6.5.4 Fits to an anisotropic scintillation pattern

Figures 6.20*c* and 6.20*d* show fits obtained allowing an anisotropic scintillation pattern with no velocity offset from the LSR. Finally, Figures 6.20*e* and 6.20*f* show fits obtained for an anisotropic scintillation pattern and allowing a screen velocity offset from the LSR. The width of the $t_{\rm ISS}$ peak, allowing all parameters to vary, is best fitted for both frequencies with $\delta {\rm v}_\alpha = -5$ km s^{-1} and $\delta {\rm v}_\delta = 0$, and when the minor axis of the scintillation pattern lies at an angle of approximately $25^\circ \pm 10^\circ$ to $\mathbf{v}_{\rm ISM}$. The best fits are found for axial ratios < 0.5. Decreasing the axial ratio below ~ 0.25 has little effect on the shape of the $t_{\rm ISS}$ annual cycle, because ${\rm v}_{\rm ISS}$ never cuts directly across the long axis of the fitted scintillation pattern (see Figure 6.16*d*). This result is consistent with what is expected from depth of the first minimum in the ACFs, which in the case of PKS 0405−385 was fitted with a highly anisotropic medium (axial ratio ~ 0.25; Rickett et al. 2002). Those sources for which $\mathbf{v}_{\rm ISS}$ at its maximum cuts across the short axis of the scintillation pattern are those most likely to scintillate rapidly.

For the best fits allowing all parameters to vary (Figures 6.20*e* and 6.20*f*), the minor axes of the scintillation pattern scale are approximately $s_0 = 4.2 \pm 0.5 \times 10^4$ km at 4.8 GHz, and $s_0 = 3.5 \pm 0.5 \times 10^4$ km at 8.6 GHz, In the case of anisotropic scattering, the typical length scale for the minor axis is the Fresnel scale reduced by a factor of $\sim \sqrt{2}$ (B.J. Rickett 2002, priv. comm.). Setting $R_\theta = 1$ and replacing s_0 with $r_{\rm F} \approx \sqrt{2} s_0$ in Equation 6.2 gives values for the screen distance of $L \approx 11.5 \pm 3$ pc at 4.8 GHz, and $L \approx 14.4 \pm 4$ pc at 8.6 GHz; very similar values to those obtained for the isotropic case.

6.5.5 Milliarcsecond-scale structure and constraints on the scintillating flux density

To obtain limits on the source brightness temperature, $T_{\rm b}$, it is necessary to know the flux density, S_c, of the scintillating component of PKS 1257−326. An upper limit on this flux density is obtained from a Target of Opportunity VLBI observation which was performed at 4.8 GHz on 2001 March 23, with Parkes, the ATCA and Mopra antennas. The antenna at Ceduna was also scheduled but failed. The LBA data were calibrated using observations of PKS 0537−441 and PKS 1519−273, which were observed at the beginning and mid-way through the observing period, respectively. Both of these sources are essentially unresolved between the angular scales of the ATCA and the three LBA baselines. Thus, the LBA antenna gain amplitudes are scaled, to an accuracy of

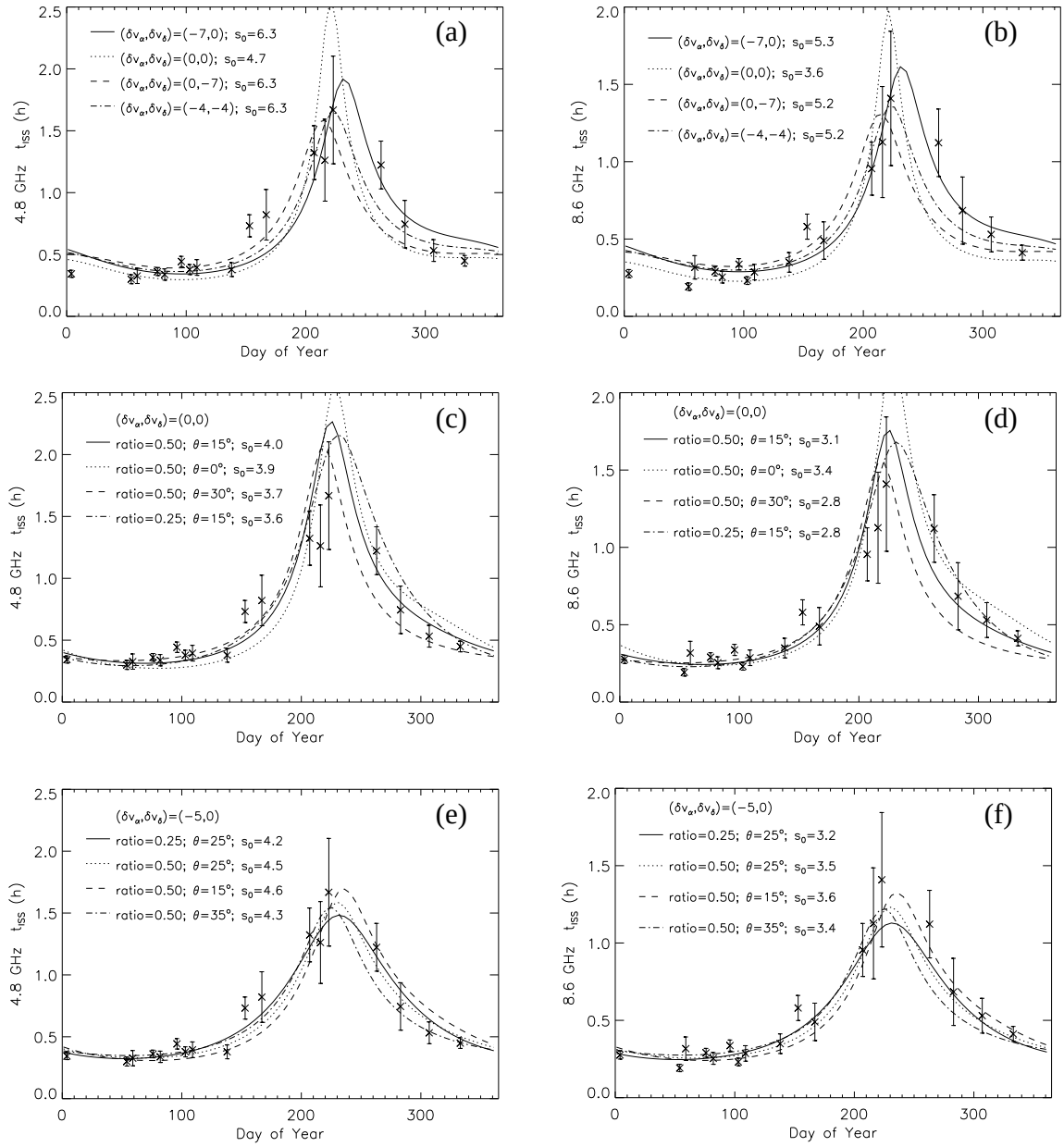

Figure 6.20: Various fits to the annual cycle in $t_{\rm ISS}$. (a) and (b) are for an isotropic source and isotropic scattering. (c) and (d) are for a medium moving with the local standard of rest (LSR), allowing an anisotropic scintillation pattern. (e) and (f) are for an ISM velocity offset from the LSR and an anisotropic pattern. Model parameters are shown on the plots. Ratio is the axial ratio of the anisotropy. $\delta {\rm v}_\alpha$ and $\delta {\rm v}_\delta$ are in units of km s^{-1}, s_0 is in units of 10^4 km. θ is the angle between $\mathbf{v}_{\rm ISM}$ and the minor axis of the scintillation pattern. See Section 6.5.4 for further explanation.

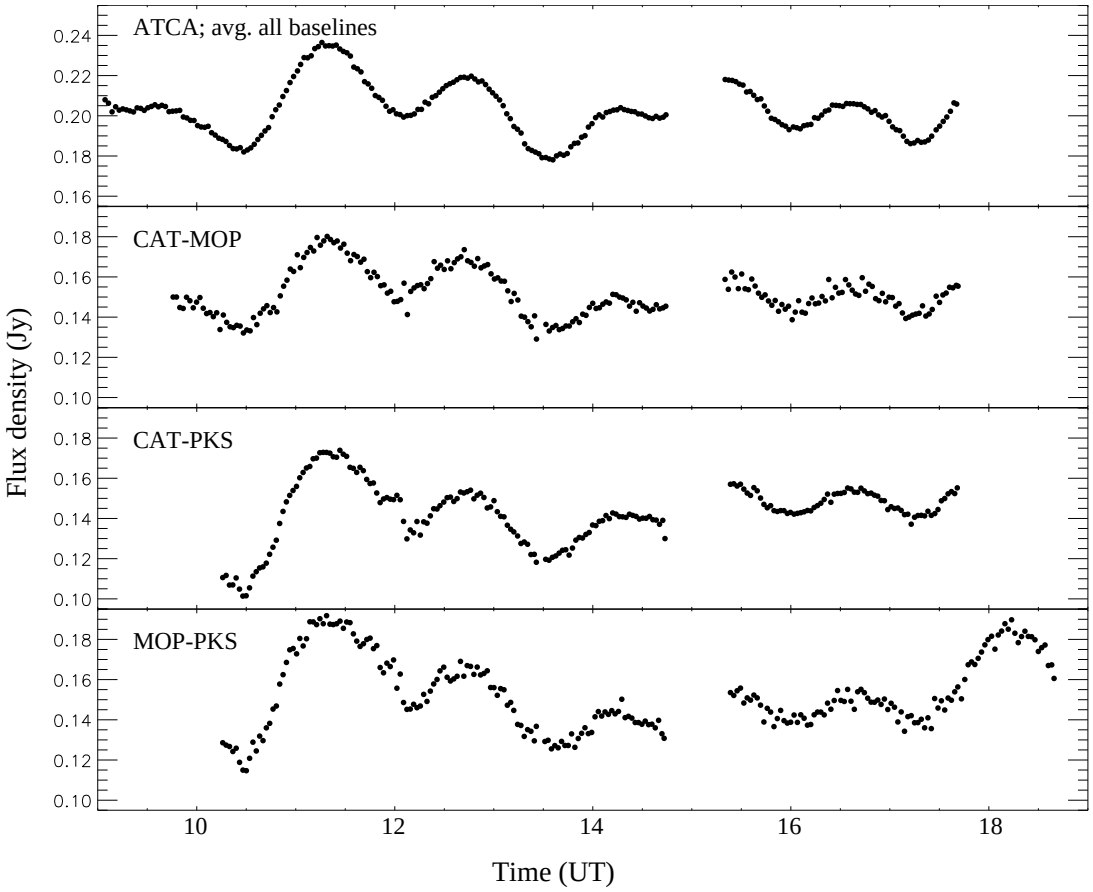

Figure 6.21: ATCA and LBA visibility amplitudes from 2001 March 23, plotted with 2-minute averaging. ATCA data averaged over all baselines are shown at the top. Below this are the flux densities on the three LBA baselines, plotted separately. CAT=Compact Array Tied array; MOP=Mopra, PKS=Parkes. Axis scales are the same in each plot, except the ordinate values are displaced by 60 mJy in the top window to show the total flux density from the ATCA.

$\sim 5\%$, using the flux densities of the calibration sources measured simultaneously with the ATCA.

Figure 6.21 shows the total flux density for PKS 1257−326 measured with the ATCA during the VLBI observation (the same data as shown in Figure 6.3), and the calibrated visibilities on the three LBA baselines. The scintillation pattern is clearly seen to be similar on all baselines, however a comparison of the average flux densities suggests that approximately 50 mJy of flux density is missing between the arcsecond scales measured by the ATCA, and the $\sim 0.1''$ angular scale of the LBA baselines.

The closure phases around the LBA triangle show a significant deviation, of a few degrees, from zero, indicating source structure on a scale of $\lesssim 0.1''$ (see Figure 6.22). An investigation was done to determine whether a simple, two component model could reproduce the observed closure phases, and if so, how well such a model could be constrained, and what would be its effect on the observed visibility amplitudes. The

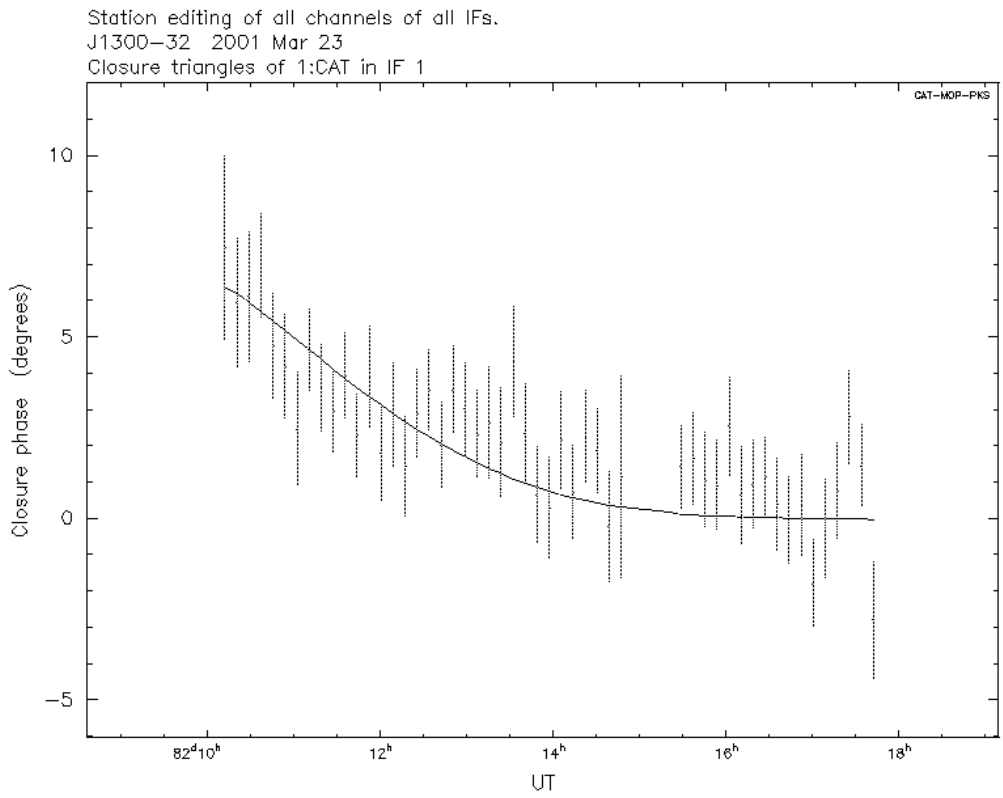

Figure 6.22: Closure phases on triangle Parkes-Mopra-Narrabri. Solid line shows the expected closure phases for a simple model of a 125 mJy point source with a second, 25 mJy point source 15 mas away at a position angle 50° west of North.

closure phase variation appears to be dominated by a slow, single "beat", indicating that most of the extended flux density is in a component within $\sim$ 20 mas of the unresolved "core" component. Also, the very close similarity between the variations observed with the ATCA and those observed on the shortest LBA baseline, Narrabri-Mopra, demonstrates that the VLBI structure must be contained within $\sim$ 30 mas of the core. A component further from the core would produce multiple beats in the closure phase. The observed closure phase variation constrains the component to be at a position angle of $\sim 50 \pm 20°$ west of North. Notably, the position angle of the milliarcsecond extension is similar to the position angle of the arcsecond-scale extended structure. The closest component to the core observed in the arcsecond scale jet (Figure 6.6) is at a position angle $\sim 25°$ west of North.

The flux density of the secondary component in the LBA data is weakly constrained to be $\sim 20 - 30$ mJy. While a unique model cannot be found from the closure phases alone, the fitted model implies a reduction in visibility amplitudes on the two longest baselines near the beginning of the observation. This is consistent with the observed deep minimum in flux density seen on the longer baselines near 10:30 UT. Figure 6.21

shows that the difference between the visibility amplitudes on each baseline is greatest early in the observation, and similarly the greatest deviation from zero in closure phase is observed at the beginning of the observation.

From the LBA results, the flux density, S_c, in the scintillating component of PKS 1257−326 can be no more than $\sim 140\,\mathrm{mJy}$. Also, S_c cannot be negative, so a lower limit on S_c is given by $S_c \geq S_\mathrm{T} - S_\mathrm{min}$, where S_T is the total average flux density and S_min is the lowest flux density observed. For some well-sampled epochs, $S_\mathrm{T} - S_\mathrm{min} \approx 50\,\mathrm{mJy}$. Thus, $50\,\mathrm{mJy} \lesssim S_c \lesssim 140\,\mathrm{mJy}$.

6.5.6 Source brightness temperature

Assuming a circularly symmetric source brightness distribution with FWHM corresponding to the Fresnel scale size, an approximate lower limit on the rest-frame brightness temperature, $T_\mathrm{b} = 4 \times 10^{12}\,\mathrm{K}$, is obtained for $S_c = 50\,\mathrm{mJy}$ and $\theta_\mathrm{S} = 40\mu\mathrm{as}$ at an observed frequency of 4.8 GHz. This requires relativistic beaming with a Doppler factor of $\mathcal{D} \gtrsim 4$ so as not to violate the Inverse Compton (IC) limited brightness temperature of $\sim 10^{12}\,\mathrm{K}$ for synchrotron radiation. If in the rest frame the source is at an equipartition brightness temperature of $\sim 2 \times 10^{11}\,\mathrm{K}$, as defined by Readhead (1994), then $\mathcal{D} \sim 20$ is required. While high, these implied Doppler factors are not inconsistent with apparent superluminal speeds found in VLBI surveys (Marscher et al., 2000; Kellermann et al., 2000). Taking $S_c = 140\,\mathrm{mJy}$ and $\theta_\mathrm{S} = 30\mu\mathrm{as}$ gives a somewhat more extreme brightness temperature of $T_\mathrm{b} = 2 \times 10^{13}\,\mathrm{K}$, with correspondingly higher Doppler factors.

In the anisotropic case, it may be that T_b could be reduced somewhat below these values if the source was, coincidentally, elongated in the same direction as the long axis of the scattering. It is interesting to note that the milliarcsecond scale jet direction is in approximately the same direction as the fitted major axis for an anisotropic scintillation pattern. However, as discussed in the next section, the μas-scale "jet" appears to be orthogonal to the mas position angle.

6.5.7 A model for the time offset between 4.8 and 8.6 GHz

The offset between the IDV patterns observed at 4.8 and 8.6 GHz, $\tau_{(4.8,8.6)}$, may be due to an offset between the central components of the source at each frequency. This might be expected if the source were jet-like on a μas scale, and optically thick between 5 and 8 GHz. The line in Figure 6.19 shows an expected annual cycle for an offset beween the two components, with projected displacement vector $D(\alpha, \delta) = (1.5, 0.9) \times 10^4$ km in components of RA and Dec, using the best-fit ISM velocity derived from the t_ISS annual cycle above. Given the large (but difficult to estimate) uncertainties in the measurement of $\tau_{(4.8,8.6)}$, this model seems a reasonable fit to the data. The fact that $\tau_{(4.8,8.6)}$ always has the same sign severely constrains the direction of the offset of the two components, and also implies that the origin in Figure 6.16*d* cannot be inside the ellipse; i.e. $\mathbf{v}_\mathrm{ISS}$ changes direction by $< 180^\circ$ over the year. This is consistent with what is expected from the annual cycle in t_ISS. Figure 6.16*d* shows contours of the

best fit scintillation pattern at each frequency, and indicates the direction of the fitted offset between the 4.8 and 8.6 GHz components. The fitted displacement vector implies that the 8.6 GHz component is centred slightly to the North and East of the 4.8 GHz component.

For a screen distance of 10 pc, the fitted displacement vector corresponds to an offset of 12μas. This order of resolution is currently unachievable by any other technique, and is comparable to that expected for proposed future space-based X-ray (Cash et al., 2000) and optical (Unwin et al., 2002) interferometry missions. An offset of this order between different frequency components may also have implications for future astrometry and geodesy programs. Assuming $H_0 = 65\,\mathrm{km\,s^{-1}\,Mpc^{-1}}$ and $q_0 = 0.5$, 12μas at z=1.256 corresponds to 0.08 pc. Such an offset could be explained as an optical depth effect due to synchrotron self-absorption in the source. In this case, the higher frequency component may be expected to emerge closer to the base of the jet, which would imply a microarcsecond-scale jet oriented in the south-west direction. This is approximately orthogonal to the milliarcsecond- and arcsecond-scale jets. Given the apparent alignment of the anisotropy with the larger scale jet, however, a small separation in this direction may not be "resolved" in the scintillation pattern. It is also possible that there may be a significant bend in the jet between the 10 mas and 10 μas scales.

Another possibility which has not been ruled out is that the frequency offset is due to a refractive effect in the ISM rather than the source itself. Further investigation of the possible frequency dependence of the offset is ongoing, using data at several frequencies between 4.8 and 9.0 GHz.

6.6 Intrinsic variability

The long-term flux density monitoring of PKS 1257−326 (Figure 6.17) suggests that, in addition to the scintillation, it is undergoing slow, intrinsic changes. Such intrinsic, pc-scale outbursts are commonly seen in flat-spectrum sources, yet there has been little change in the scintillating flux density. This is despite the optically thick spectrum of the slowly varying source, and suggests that the μas core does not lie directly behind what is presumably an expanding pc-scale jet, as might be expected if the scintillating component were the "core" at the base of the pc-scale jet. In other words, the pc-scale outburst may be occurring in a separate emitting region, further out from the core in a component too large to scintillate.

It is interesting to compare the brightness temperature inferred from the long-term intrinsic variability, with that obtained from the ISS model. For PKS 1257−326, a steady increase in the mean flux density at 8.6 GHz of $\Delta\bar{S} = 0.14$ Jy was observed over a period of 440 days, while over the same time the mean 4.8 GHz flux density increased by $\Delta\bar{S} = 0.08$ Jy. The simple approach of taking these values of $\Delta\bar{S}$ to be the flux density of the slowly varying component at each frequency, and observed variability time-scale $t_{\rm int} = 440$ days, gives a variability brightness temperature (in the source proper frame), $T_{\rm b}^{\rm var}$, of 3×10^{12} K from the 8.6 GHz long-term variability, and $T_{\rm b}^{\rm var} =$

6×10^{12} K from the 4.8 GHz long-term variability (Lähteenmäki & Valtaoja, 1999). For relativistically beamed radiation with Doppler factor $\mathcal{D}$, the inferred variability brightness temperature $T_{\rm b}^{\rm var}$ is related to the source rest-frame brightness temperature $T'_{\rm b}$, by $T_{\rm b}^{\rm var} = \mathcal{D}^3 T'_{\rm b}$. (Where $T_{\rm b}$ is calculated from an angular size which has been measured *directly*, or estimated from an ISS model as in Section 3 above, then $T_{\rm b} = \mathcal{D}T'_{\rm b}$.) Taking the $\mathcal{D}^3$ dependence into account, the intrinsic brightness temperature inferred from the long-term variability is smaller than that calculated from the modelled angular size of the scintillating component. This is consistent with the long-term variability occurring in a larger region, separate from the scintillating component, and the lack of any significant change in the scintillating flux density.

In the μas-scale component, which may be the base of the jet, the brightness temperature is high, implying $4 < \mathcal{D} \lesssim 40$, but in the pc-scale "jet", the inferred $T_{\rm b}$ is lower and the Doppler factor significantly lower, ~ 2. This could be explained if the jet decelerates rapidly between μas and mas scales, or alternatively, if the pc-scale jet reflects a pattern speed which may well be less than the underlying fluid motion.

6.7 Significance of the fast scintillators

The three fast scintillators PKS 0405−385, J1819+3845, and PKS 1257−326, are valuable because their rapid scintillation time-scale allows one to characterize the statistics of the underlying scintillation process over a typical 12-hour observing session; one observes more stastically independent "scints" per unit time compared with slower scintillators. This is important because the dominant source of error in modelling the structure of a scintillating source is in characterizing the properties of the scintillation process itself. Moreover, in their periods of rapid variability it proved possible to make the pattern time delay measurements, crucial in establishing the ISS origin (Jauncey et al. 2000b; Dennett-Thorpe & de Bruyn 2002; and this thesis, Section 6.3), since this is not possible for the more usual, slower scintillating sources with characteristic time scales of order a day. These three rapidly scintillating sources proved invaluable in making the transition from IDV to ISS. Viewed from an IDV perspective, their properties appear extreme. From a scintillation perspective, however, are these sources really so extreme?

The answer lies in the reasons for their rapid scintillation. The characteristic time-scale for scintillation is $t_{\rm ISS} = s_{\rm ISS}/{\rm v}_{\rm ISS}$, where $s_{\rm ISS}$ is the scintillation length scale and ${\rm v}_{\rm ISS}$ is the bulk velocity of the scattering plasma in the observer's frame of rest. If an annual cycle is observed in $t_{\rm ISS}$, it follows that the scattering plasma velocity must be close to the 30 km s^{-1} of the Earth's orbital speed. As discussed in Section 3, for an observed frequency ν in the weak scattering regime, $s_{\rm ISS}$ is related to the Fresnel scale, $r_{\rm F}$, which scales with screen distance L as $r_{\rm F} \propto \sqrt{L}$. $s_{\rm ISS}$ also depends on the source angular size, $\theta_{\rm S}$, in the case where this exceeds the angular Fresnel scale, such that $s_{\rm ISS} \sim L\theta_{\rm S}$. For most extragalactic sources, the relation of time scale to screen distance lies between a square root and a linear dependence (Rickett et al., 2002). It follows that the fast scintillators, those with small $t_{\rm ISS}$, will be those scintillating sources which

are to be found behind very nearby scattering screens. The evidence in support of this is the screen distances of $\lesssim 30$ pc found for J1819+3845 (Dennett-Thorpe & de Bruyn, 2000) PKS 0405−385 (Rickett et al., 2002), and here, for PKS 1257−326.

From the scintillation perspective, these fast variables are extreme in the sense that they are to be found behind nearby scattering material, not in that there is any inherently extreme property in the sources themselves. There is no evidence for anything intrinsically unusual about PKS 1257−326 which sets it apart from other flat-spectrum, radio-loud quasars. In fact, its radio properties are less extreme than might be expected for the more common, slower scintillators. Since the angular size required for a source to scintillate in the ISM is set by the angular size of the first Fresnel zone, those sources which show large variations with longer characteristic time scales are more likely to be found behind scattering screens at much larger distances, and hence with smaller angular sizes and correspondingly higher brightness temperatures.

There are also implications for the properties of the interstellar medium. The small number of fast scintillators found to date suggests that there are few regions of the Galaxy where such nearby screens may be found. Moreover, as noted above, the presence of a nearby screen relaxes the constraints on the angular size necessary for a source to scintillate. Thus there will likely be more sources with components with angular sizes of order 20 μas, which can scintillate through a screen at $L \lesssim 30$ pc, than there will be sources with 5–10 μas angular sized components to scintillate through a screen at, say, 500 pc. In this regard, it is notable that the two long-lived fast scintillators, J1819+3845 and PKS 1257−326, are the two weakest IDV sources reported. If the above is correct, then a deep, unbiased scintillation survey would be expected to confirm the low numbers of fast scintillators. Alternatively, the discovery of more such rapid scintillators can reveal the presence of such nearby scattering material in the Galaxy. The recently undertaken *Micro-Arcsecond Scintillation-Induced Variability* (MASIV) Survey of 700, flat-spectrum radio sources over the whole northern sky with the VLA (Lovell et al., 2002, 2003) observations, are expected to reveal the relative importance of intrinsic source properties, and properties of the Galactic ISM, for scintillation.

6.8 Summary

The main results from the observations of PKS 1257−326, and some of the implications of these results for investigations of scintillating sources in general, are summarised below.

- PKS 1257−326 is a rapidly scintillating radio source with similar properties to the other rapid IDVs, in particular J1819+3845 (Dennett-Thorpe & de Bruyn, 2000) and PKS 0405−385 (Kedziora-Chudczer et al., 1997; Rickett et al., 2002).

- It is remarkable that the scintillating components in many sources are both remarkably small, on the order of 0.1 pc, but at the same time long lived. For

example, 0917+624 showed scintillation for $\gtrsim 15$ years before ceasing to scintillate (Fuhrmann et al., 2002), J1819+3845 has been scintillating rapidly for ~ 4 years at least, and PKS 1257−326 has apparently been scintillating for at least 7 years.

- Monitoring PKS 1257−326 over more than a year reveals a clear annual cycle in the characteristic time-scale of variability.
- The annual cycle provides unequivocal evidence for a scintillation origin of the IDV observed in this source.
- Modelling the annual cycle provides strong evidence for highly anisotropic scattering in the ISM.
- The very rapid variability is most likely due to scintillation in a nearby screen, only ~ 10 to 15 pc from the sun.
- Assuming a source size equal to the Fresnel scale at the distance of the screen, the implied brightness temperature is then $4 \times 10^{12}\,\mathrm{K} \lesssim T_\mathrm{b} \lesssim 2 \times 10^{13}\,\mathrm{K}$, which is high, but not entirely unacceptable for relativistically beamed radiation from a jet.
- A time offset is observed between the scintillation patterns at each frequency, which itself exhibits an annual cycle. This we tentatively model as an offset due to opacity effects in the source on a scale of $\sim 10\mu$as, or ~ 0.1 pc at the source.
- A time delay of ~ 8 minutes has been observed between the variability pattern arrival times at two widely-spaced telescopes, the VLA and the ATCA. Measurement of the pattern time delay at several epochs can be used to *directly* constrain the two-dimensional structure of the scintillation pattern. Parameters fitted to the first epoch time delay measurement are consistent with the results of fitting to the annual cycle in characteristic time-scale. The time delay measurement also provides evidence for a highly anistropic pattern.
- There are much slower flux density changes in the pc-scale structure of the source, but as yet these do not appear to be mirrored in any obvious changes in the microarcsecond sized component responsible for the IDV.
- A difference between the inferred Doppler factor of the scintillating sub-pc scale component, and that of the component showing slow, intrinsic variability, suggests either a rapidly decelerating jet, or else that the pc-scale jet represents a pattern speed rather than the speed of the underlying flow.
- Continued monitoring of PKS 1257−326 is ongoing, with the following aims: (i) to better constrain the time-scale during the slow-down period, and hence more tightly constrain the scale and structure of the scintillation pattern; (ii) to independently constrain the scintillation parameters and source structure from

two more simultaneous ATCA/VLA time delay measurements; (iii) to investigate the frequency dependence, and possible time-dependent changes, of the observed offset between the 4.8 and 8.6 GHz scintillating components; and (iv) to investigate the relationship between the scintillating component and long-term, intrinsic changes in the source. High-resolution VLBI observations are also planned to investigate the pc-scale source structure and evolution.

- For sources scintillating in the weak scattering regime which show large variations on timescales of the order of a day, the scattering screens may be at much larger distances of several hundred pc. This requires smaller source sizes, so in fact these slower scintillators may have higher implied brightness temperatures than the very rapid scintillators.

- Observations of scintillating sources provide a method of achieving μas resolution at cm-wavelengths with modest radio telescopes, resolution comparable with that proposed for future space-based optical and X-ray interferometers.